

Predictions for detecting BHNS and other double compact objects binaries with LISA

T. WAGG ,¹ F. BROEKGAARDEN ,¹ AND S. E. DE MINK ,^{1,2}

¹Center for Astrophysics — Harvard & Smithsonian, 60 Garden Street, Cambridge, MA 02138, USA

²Anton Pannekoek Institute for Astronomy and GRAPPA, University of Amsterdam, NL-1090 GE Amsterdam, The Netherlands

(Received April 10, 2021)

ABSTRACT

Keywords: LISA, black hole, neutron star, binary

1. INTRODUCTION

Since the first direct detection of gravitational waves by the LIGO scientific collaboration (Abbott et al. 2016), the number of black hole (BH) binaries and neutron star (NS) binaries detected by ground-based detectors has rapidly grown (Abbott et al. 2019, 2020b). These detections offer exciting insights into the endpoints of massive stars and the investigation of population statistics provides an essential tool for constraining uncertainties in binary evolution and predicting distributions of observable parameters for different double compact object (DCO) types.

The Laser Interferometer Space Antenna (LISA, Amaro-Seoane et al. 2017) presents an exciting new lens through which to view the realm of gravitational waves. In the same way that radio telescopes produce a different, but complementary, view of the sky than optical telescopes, LISA will detect a different and complementary population of gravitational wave sources. LISA will observe binaries at lower orbital frequencies than ground-based detectors ($10^{-5} \lesssim f/\text{Hz} \lesssim 10^{-1}$) and therefore focus on the inspiral phase of stellar mass binaries rather than the merger. This will allow LISA to detect, and possibly localise a binary on the sky, far

in advance of the merger, which presents an opportunity for both multimessenger detections to search for electromagnetic counterparts and multiband detections that would better constrain binary characteristics (e.g. [Gerosa et al. 2019](#)). In addition, DCOs may still have significant eccentricity in the LISA band and measurements of eccentricity may provide further constraints on binary evolution (e.g. [Breivik et al. 2016](#)), differentiate between formation channels and distinguish between DCO types. The maximum detectable distance for stellar mass sources in LISA is significantly lower than in ground-based detectors since the gravitational wave signal is weaker during the inspiral than at the merger. This means that LISA stellar mass sources are an excellent probe for our galaxy’s history and evolution.

Traditionally, investigations into detecting stellar mass sources with LISA focus on double white dwarf (WDWD) binaries (Ruiter et al. 2010; Yu & Jeffery 2010; Nissanke et al. 2012; Korol et al. 2017; Lamberts et al. 2018). However, whilst NS and BH binaries are rare, they provide an excellent probe for the endpoints of massive stars.

Double black hole (BHBH) binaries are the dominant source in ground-based gravitational wave detections

and several studies have tried to model the black hole mass function as well as identify the pair instability mass gap (e.g. Baxter et al. 2021). In contrast, BHBHs in LISA are not biased towards higher masses and instead will probe lower mass black holes, potentially offering insight about the presence of a lower mass gap between neutron stars and black holes.

Galactic double neutron star (NSNS) binaries have been observed with electromagnetic signals for several decades (e.g. Hulse & Taylor 1975) and more recently the mergers of NSNS binaries with ground-based gravitational wave detectors have been observed (e.g. Abbott et al. 2017). The detection of a NSNS in LISA in which at least one NS is a pulsar could connect these two populations as the binary could be observed from inspiral to merger. NSNS binaries are excellent sources for understanding the origin of r-process elements (e.g. Eichler et al. 1989) as well as the electromagnetic counterparts to gravitational wave signal such as kilonovae (e.g. Metzger 2017), short gamma-ray bursts (e.g. Gompertz et al. 2020), radio emission (e.g. Hotokezaka et al. 2016) and neutrinos (e.g. Kyutoku et al. 2018).

One particularly interesting and elusive gravitational wave source is a black hole neutron star binary (BHNS). Of all the events detected by ground-based detectors, none can be confidently attributed to the merger of a black hole and a neutron star, though several events such as GW190425 and GW190814 have not been ruled out as a BHNS merger (Abbott et al. 2020a,c). Predictions for the merger rate of BHNSs range across three orders of magnitude (e.g. Broekgaarden et al. 2021) so the number of detections in LISA will be important in reducing this uncertainty, thereby refining our understanding of the remnants and evolution of massive stars. These binaries are expected to have similar electromagnetic counterparts to NSNSs and so can be studied in the same way. A distinctly exciting possibility is the detection of a pulsar–BH system or millisecond pulsar–BH system as these could be observed not only by gravitational wave detectors, but also radio telescopes such as MeerKAT and SKA, which will help to constrain uncertain binary evolution processes (Chattopadhyay et al. 2020).

The detection of DCOs with LISA has been investigated in many previous studies through a combination of population synthesis and Milky Way modelling. Previous studies that investigate BHBH, BHNS and NSNS binaries, as opposed to the numerous WDWD population, are still rare. Earlier work has used a variety of population synthesis codes, Milky Way models and LISA specifications, resulting in a wide range of predictions (Nelemans et al. 2001; Liu 2009; Belczynski et al.

2010; Liu & Zhang 2014; Lamberts et al. 2019; Lau et al. 2020; Breivik et al. 2020; Sesana et al. 2020).

We build upon previous efforts but will several important improvements. We explore the effect of varying binary physics assumptions by repeating our analysis for 15 different models and comparing the effect on the detection rate and distributions of source parameters. We use a model for the Milky Way that is dependent on the chemical enrichment history and calibrated on the latest GAIA and APOGEE surveys (Frankel et al. 2018). In contrast to many previous works, we provide a full treatment of the eccentricity of detectable sources both for the inspiral evolution as well as gravitational wave signal during the LISA mission. Moreover, our binary population synthesis simulation is the most extensive of its kind, with 750 million binaries (one million binaries for each of 50 metallicity bins and 15 physics variations) evolved to produce the DCO populations used in this work (Broekgaarden et al. 2021). In addition, we use the adaptive sampling algorithm STROOPWAFEL to further reduce our sampling noise (Broekgaarden et al. 2019).

In this paper, we present the most extensive simulations to date for predictions of the detection rate and distribution of binary properties (masses, frequency, eccentricity, distance, merger time) of BHBH, BHNS and NSNS binaries formed through isolated binary evolution in the Milky Way. We explore 15 different models of physical assumptions in our population synthesis model and how the changes in these assumptions alter our results. We also discuss the effect of extending the LISA mission length and the possibility of distinguishing detections.

In Section 2, we describe our methods for synthesising a population of binaries, the variations of physical assumptions that we consider, how we simulate the Milky Way distribution of DCOs and our methods for calculating a detection rate for LISA. We present our main results in Section 3, analysing our findings for each DCO type and variation of physical assumptions. In Section 4 we discuss these results. In Section 5, we compare and contrast our methods and findings to previous work and finish with our conclusions in Section 6.

2. METHOD

2.1. *Binary population synthesis*

We use a population of binaries synthesised using the rapid population synthesis code COMPAS (Stevenson et al. 2017; Vigna-Gómez et al. 2018; Stevenson et al. 2019). COMPAS broadly follows the approach of other codes, such as BSE (Hurley et al. 2002). Each sampled binary is initialised as a zero-age main sequence

(ZAMS) binary and each component star is evolved using the single star evolution fitting formulae from Hurley et al. (2000) to the models of Pols et al. (1998). In addition, we apply the adaptive importance sampling algorithm STROOPWAFEL (Broekgaarden et al. 2019) to improve the yield of our sample. This algorithm increases the prevalence of target DCOs (BHBH, BHNS and NSNS binaries in this case) in the sample and assigns each a weight, w , which represents the probability of drawing it without STROOPWAFEL in effect.

2.1.1. Population overview

The population of double compact objects used in this study was synthesised by Broekgaarden et al. (2021). One million binaries, $N_{\text{binary}} \sim 10^6$, were simulated for each of 50 metallicity bins equally spaced in log space with $Z \in [0.0001, 0.022]$, where Z is the mass fraction of heavy elements. These bins span the allowed metallicities range for the original fitting formulae on which COMPAS is based (Hurley et al. 2000). This is repeated for 14 physics variations (see Section 2.1.4) and so in total 750 million binaries were simulated.

2.1.2. Initial conditions

Each binary is sampled from initial distributions for the primary and secondary masses as well as the separation. The primary mass, or the mass of the initially more massive star, is restricted to $m_1 \in [5, 150] M_\odot$ and drawn from the Kroupa (2001) Initial Mass Function (IMF), therefore $p(m_1) \propto m_1^{-2.3}$. The secondary mass is drawn using the mass ratio of the binary, which we assume to be uniform on $[0, 1]$, therefore $p(q) = 1$ (consistent e.g. with Sana et al. 2012). We additionally restrict $m_2 \geq 0.1 M_\odot$, since this is approximately the minimal mass for a main sequence star. We assume that the initial separation follows a flat in the log distribution with $p(a_i) \propto 1/a_i$ and $a_i \in [0.01, 1000] \text{ AU}$ (Öpik 1924; Abt 1983). We assume that all binaries are circular at birth to reduce the dimensions of initial parameters. Since we focus on post-interaction binaries which will have circularised during mass transfer this is a reasonable assumption and is likely not critical for predicting detection rates (Hurley et al. 2002; de Mink & Belczynski 2015).

For each metallicity Z , we have a sample of binaries, each with a set of parameters

$$\mathbf{b}_{Z,i} = \{m_1, m_2, a_{\text{DCO}}, e_{\text{DCO}}, t_{\text{evolve}}, t_{\text{inspiral}}, w\}, \quad (1)$$

for $i = 1, 2, \dots, N_{\text{binary}}$, where m_1 and m_2 are the primary and secondary masses, a_{DCO} and e_{DCO} are the semi-major axis and eccentricity at the moment of double compact object (DCO) formation, t_{evolve} is the time

between the binary's zero-age main sequence and DCO formation, t_{inspiral} is the time between DCO formation and gravitational-wave merger, w is the adaptive importance sampling weight assigned by STROOPWAFEL. We sample from these sets of parameters when creating synthetic galaxies.

2.1.3. Physical assumptions in fiducial model

In this section we briefly summarise the main physical assumptions in our fiducial model. For more details see Section 2.1.2 and Table 1 of Broekgaarden et al. (2021).

Mass Transfer: In determining the stability of mass transfer we use the ζ -prescription, which compares the radial response of the star with the response of the Roche lobe radius to the mass transfer (e.g. Hjellming & Webbink 1987). The mass transfer efficiency, $\beta = \Delta M_{\text{acc}}/\Delta M_{\text{don}}$, is defined as the fraction of the mass transferred by the donor that is actually accreted by the accretor. We limit the maximum accretion rate for stars to $\Delta M_{\text{acc}}/\Delta t \leq 10M_{\text{acc}}/\tau_{\text{KH}}$, where τ_{KH} is the Kelvin-Helmholtz timescale of the star (Paczyński & Sienkiewicz 1972; Hurley et al. 2002). The maximum accretion rate for double compact objects is limited to the Eddington accretion rate. If more mass than these rates is accreted then we assume that the excess is lost through isotropic re-emission in the vicinity of the accreting star, thus varying β (e.g. Massevitch & Yungelson 1975; Soberman et al. 1997). We assume that all mass transfer phases from a stripped post-helium-burning-star (case BB) onto a neutron star or black hole are unstable (Tauris et al. 2015).

Common Envelope: A common envelope phase follows dynamically unstable mass transfer and we parameterise this using the α - λ prescription from Webbink (1984) and de Kool (1990). We assume $\alpha = 1$, such that all of the gravitational binding energy is available for the ejection of the envelope. For λ we use the fitting formulae from Xu & Li (2010a,b). We assume that any Hertzsprung gap donor stars that initiate a common envelope phase will not survive this phase due to a lack of a steep density gradient between the core and envelope (Taam & Sandquist 2000; Ivanova & Taam 2004). This follows the ‘pessimistic’ common envelope scenario (c.f. Belczynski et al. 2007). We remove any binaries where the secondary immediately fills its Roche lobe upon the conclusion of the common envelope phase as we treat these as failed common envelope ejections.

Supernovae: We draw the remnant masses and natal kick magnitudes from different distributions depending on the type of supernova that occurs. For stars undergoing a general core-collapse supernova, we use the *delayed* supernova remnant mass prescription from Fryer

et al. (2012). The *delayed* prescription does not reproduce the neutron star black hole mass gap and we use this as our default as it has been shown to provide a better fit for observed populations of DCOs (e.g. Vigna-Gómez et al. 2018). We draw the natal kick magnitudes from a Maxwellian velocity distribution with a one-dimensional root-mean-square velocity dispersion of $\sigma_{\text{rms}}^{1D} = 265 \text{ km s}^{-1}$ (Lyne & Lorimer 1994; Hobbs et al. 2005).

We assume that stars with helium core masses between $1.6\text{--}2.25 M_\odot$ (Hurley et al. 2002) experience electron-capture supernovae (Nomoto 1984, 1987; Ivanova et al. 2008). We set all remnant masses to $1.26 M_\odot$ in this case as an approximation of the solution to Equation 8 of Timmes et al. (1996). For these supernovae, we set $\sigma_{\text{rms}}^{1D} = 30 \text{ km s}^{-1}$ as in Pfahl et al. (2002) and Podsiadlowski et al. (2004).

We assume that stars that undergo case BB mass transfer experience extreme stripping which leads to an ultra-stripped supernova (Tauris et al. 2013, 2015). For these supernovae we calculate the remnant mass using the Fryer et al. (2012) prescription and use $\sigma_{\text{rms}}^{1D} = 30 \text{ km s}^{-1}$ (as with electron-capture supernovae).

Stars with helium core masses between $60\text{--}135 M_\odot$ are presumed to undergo a pair-instability, or pulsational pair-instability supernova (e.g. Woosley et al. 2007; Farmer et al. 2019). We follow the prescription from Marchant et al. (2019) as implemented in (Stevenson et al. 2019) for these supernovae.

We assume that kicks are isotropic in the frame of the collapsing star. The maximum neutron star mass is predicted to be between $2\text{--}3 M_\odot$ (e.g. Kalogera & Baym 1996; Fryer et al. 2015; Margalit & Metzger 2017). We adopt a maximum neutron star mass of $2.5 M_\odot$ for the fiducial model and change the Fryer et al. (2012) prescription accordingly.

2.1.4. Physical assumptions in other models

In addition to our fiducial model, we explore 14 other models which change various aspects of the mass transfer, common envelope and supernova physics assumptions in order to assess their effect on the overall double compact object detection rates and distributions. Each of the models varies a single physics assumption (fiducial assumptions are outlined in Section 2.1.3) and these are outlined in Table 1.

Models B-E focus on changes to the mass transfer physics. We explore the effect of fixing the mass transfer efficiency β to a constant value, rather than allowing it to vary based on the maximum accretion rate, in models B, C, D, in which we set the value of β to 0.25, 0.5 and 0.75 respectively. In model E we investigate the conse-

quence of assuming that case BB mass transfer onto a neutron star or black hole is always stable rather than always unstable.

Models F-H focus on altering the common envelope physics. We change the common envelope efficiency parameter in models F and G to $\alpha = 0.5$ and 2.0 respectively. In model H, we relax our restriction that Hertzsprung gap donor stars cannot survive common envelope events, thereby following the ‘optimistic’ common envelope scenario.

Finally, models I-O make changes related to our assumptions about supernova physics. Model I uses the alternate *rapid* remnant mass prescription from Fryer et al. (2012) instead of the *delayed* prescription. We change the maximum neutron star mass in models J and K to 2 and $3 M_\odot$ respectively to account for the range of predicted maximum neutron star masses. Model L removes the implementation of pair-instability and pulsational pair-instability supernovae. In models M and N we decrease the root-mean-square velocity dispersion for core-collapse supernovae to explore the effect of lower kicks. Finally, model O removes the natal kick for all black holes.

Model	Physics Variation
A	–
B	Fixed mass transfer efficiency of $\beta = 0.25$
C	Fixed mass transfer efficiency of $\beta = 0.5$
D	Fixed mass transfer efficiency of $\beta = 0.75$
E	Case BB mass transfer is always unstable
F	CE efficiency parameter $\alpha = 0.5$
G	CE efficiency parameter $\alpha = 2$
H	HG donor stars initiating a CE survive CE
I	Fryer rapid SN remnant mass prescription
J	Maximum NS mass is fixed to $2 M_\odot$
K	Maximum NS mass is fixed to $3 M_\odot$
L	PISN and pulsational-PISN not implemented
M	$\sigma_{\text{rms}}^{1D} = 100 \text{ km s}^{-1}$ for core-collapse supernova
N	$\sigma_{\text{rms}}^{1D} = 30 \text{ km s}^{-1}$ for core-collapse supernova
O	Black holes receive no natal kick

Table 1. Adapted from Broekgaarden et al. (2021, Table 2), a description of the 15 binary population synthesis models used in this study. A is the fiducial model, B-E change mass transfer physics, F-H change common envelope physics and I-O change supernova physics.

2.2. Galaxy synthesis

In order to produce a detection rate of DCOs with statistical uncertainties, we create a series of random instances of the Milky Way, each populated with a sub-

sample of the synthesised binaries. For the distribution of the binaries, we make the simplification that the Milky Way is composed of only a single disc. We do not find that adding other components would significantly alter our results.

Most previous studies that predict a detection rate for LISA place binaries in the Milky Way independently of their age or evolution. We improve upon this as the first study to use an analytical model of the Milky Way that takes into account the galaxy's enrichment history.

2.2.1. Milky Way disc model

For the Milky Way thin disc, we use the model from Frankel et al. (2018). The authors developed this model in order to measure the global efficiency of radial migration in the Milky Way. They did this by fitting the model to a sample of red clump stars measured with APOGEE (Majewski et al. 2017) and Gaia (Gaia Collaboration et al. 2016). The result of this work is a model for the Milky Way that is calibrated to observations and includes the star formation history, radial birth profile and chemical enrichment history of the galaxy. We can therefore use this model to place binaries randomly in space and time and match these positions to a metallicity.

The star formation history is given by the following (Frankel et al. 2018, Eq. 2)

$$p(\tau) \propto \exp\left(-\frac{(\tau_m - \tau)}{\tau_{\text{SFR}}}\right), \quad (2)$$

where τ is the lookback time (the amount of time elapsed between the binary's zero-age main sequence and today), $\tau_m = 12$ Gyr is the assumed age of the Milky Way and $\tau_{\text{SFR}} = 6.8$ Gyr was fit by Frankel et al. (2018). The radial birth profile of the galaxy is conditional upon its age and is given as (Frankel et al. 2018, Eq. 5)

$$p(R_0|\tau) = \exp\left(-\frac{R_0}{R_{\text{exp}}(\tau)}\right) \cdot \frac{R_0}{[R_{\text{exp}}(\tau)]^2}, \quad (3)$$

where R_0 is the birth Galactocentric radius, and¹

$$R_{\text{exp}}(\tau) = 4 \text{ kpc} \left(1 - \alpha_{R_{\text{exp}}} \left(\frac{\tau}{8 \text{ Gyr}}\right)\right), \quad (4)$$

where $\alpha_{R_{\text{exp}}} = 0.3$ was fit by Frankel et al. (2018). Finally, the metallicity-radius-time relation is given as (Frankel et al. 2018, Eq. 7)

$$\begin{aligned} [\text{Fe}/\text{H}](R, \tau) &= F_m + \nabla[\text{Fe}/\text{H}]R \\ &\quad - \left(F_m + \nabla[\text{Fe}/\text{H}]R_{[\text{Fe}/\text{H}] = 0}^{\text{now}}\right)f(\tau), \end{aligned} \quad (5)$$

¹In $R_{\text{exp}}(\tau)$, we use 4 kpc instead of 3 kpc for the 0 Gyr exponential scale-length of the disc as it provides a better fit (correspondence with Neige Frankel)

where

$$f(\tau) = \left(1 - \frac{\tau}{\tau_m}\right)^{\gamma_{[\text{Fe}/\text{H}]}} , \quad (6)$$

$F_m = -1$ dex is the metallicity of the gas at the center of the disk at $\tau = \tau_m$ and $\nabla[\text{Fe}/\text{H}] = -0.075 \text{ kpc}^{-1}$, $R_{[\text{Fe}/\text{H}] = 0}^{\text{now}} = 8.7 \text{ kpc}$ and $\gamma_{[\text{Fe}/\text{H}]} = 0.3$ are fit by Frankel et al. (2018). We can convert this to our representation of metallicity using (e.g Bertelli et al. 1994)

$$\log Z = 0.977[\text{Fe}/\text{H}] + \log(Z_\odot). \quad (7)$$

Additionally, since the Frankel model does not treat the vertical structure of the Milky Way disc, we can supplement it with the vertical distribution from McMillan (2011),

$$p(|z|) = \frac{1}{z_d} \exp\left(-\frac{z}{z_d}\right), \quad (8)$$

where z is the height above the Galactic plane and $z_d = 0.3 \text{ kpc}$. Equations 2-8 summarise the model that we use for the Milky Way disc and we illustrate these distributions in Fig. 1.

2.2.2. Combining population and galaxy synthesis

For each Milky Way instance, we randomly sample the following set of parameters

$$\mathbf{g}_i = \{\tau, R, Z, z, \theta\} \quad (9)$$

for $i = 1, 2, \dots, N_{\text{MW}}$, where we set $N_{\text{MW}} = 10^5$, τ, R, Z and z are defined and sampled using Eq. 2-8, θ is the polar angle sampled uniformly on $[0, 2\pi)$ and Z is the metallicity. Figure 1 shows an example of a random Milky Way instance created with these distributions. This shows how these distributions translate to positions in the Milky Way and illustrates the gradient in metallicity over radius.

We match each set of galaxy parameters \mathbf{g}_i , to a random set of binary parameters $\mathbf{b}_{Z,i}$, by randomly drawing a set of binary parameters from the closest metallicity bin to the metallicity in \mathbf{g}_i .

Each binary is likely to move from its birth orbit. Although all stars in the Galactic disc experience some amount of radial migration (Sellwood & Binney 2002; Frankel et al. 2018), double compact objects generally experience stronger dynamical evolution as a result of the effects of both Blaauw kicks from instantaneous symmetric mass loss (Blaauw 1961) and natal kicks from asymmetric supernovae (Hobbs et al. 2005).

The magnitude of the systemic kicks are typically small compared to the initial circular velocity of a binary at each Galactocentric radius. Therefore, kicks will not significantly alter the overall distribution of their positions. Given this, and for the sake of computational efficiency, we do not account for the displacement due to systemic kicks in our analysis.

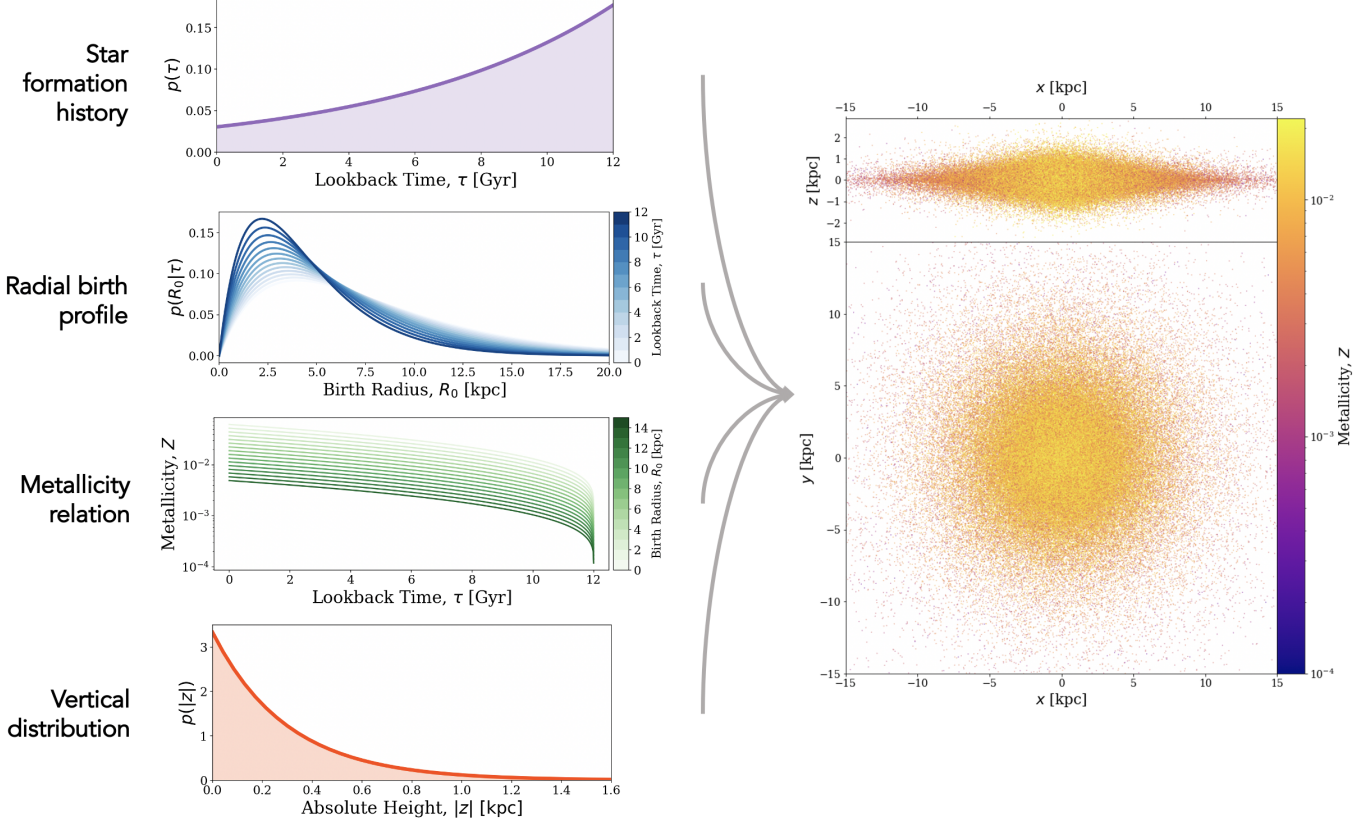


Figure 1. A schematic showing how we create a mock Milky Way disc. On the left, we show the various distributions presented in Frankel et al. (2018) and McMillan (2011). On the right, we show an example instance of the Milky Way with 10^5 binaries shown as points. The colour of each point represents its metallicity (with $Z \in [0.0001, 0.022]$). The top panel shows a side-on view and the bottom panel shows a view from above.

2.3. Gravitational wave detection

We use the Python package [LEGWORK](#) to evolve binaries and calculate their LISA detectability. For a full derivation of the equations given below please see the [LEGWORK](#) release paper (Wagg et al. in prep) or [documentation](#).

2.3.1. Inspiral evolution

Each binary loses orbital energy to gravitational waves throughout its lifetime. This causes the binary to shrink and circularise over time. In order to assess the detectability of a binary, we need to know its eccentricity and frequency at the time of the LISA mission. For each binary in our simulated Milky Way, we know that the time from DCO formation to today is $\tau - t_{\text{evolve}}$ and that the initial eccentricity and semi-major axis are e_{DCO} and a_{DCO} . We find the eccentricity of the binary at the start of the LISA mission, e_{LISA} , by numerically integrating its time derivative (Peters 1964, Eq. 5.13) given the initial conditions. This additionally can be converted to the semi-major axis at the start of LISA, a_{LISA} (Peters 1964, Eq. 5.11), which in turn gives the orbital frequency, $f_{\text{orb,LISA}}$, by Kepler's third law.

2.3.2. Binary detectability

We define a binary as detectable if its gravitational wave signal has a signal-to-noise ratio of greater than 7 (e.g. Breivik et al. 2020; Korol et al. 2020). The sky-, polarisation- and orientation-averaged signal-to-noise ratio, ρ , of an inspiraling binary can be calculated with the following (e.g. Finn & Thorne 2000)

$$\rho^2 = \sum_{n=1}^{\infty} \int_{f_{n,i}}^{f_{n,f}} \frac{h_{c,n}^2}{f_n^2 S_n(f_n)} df_n, \quad (10)$$

where n is a harmonic of the gravitational wave signal, $f_n = n \cdot f_{\text{orb}}$ is the frequency of the n^{th} harmonic of the gravitational wave signal, f_{orb} is the orbital frequency, $S_n(f_n)$ is the LISA sensitivity curve at frequency f_n (e.g. Robson et al. 2019) and $h_{c,n}$ is the characteristic strain of the n^{th} harmonic, given by (e.g. Barack & Cutler 2004)

$$h_{c,n}^2 = \frac{2^{5/3}}{3\pi^{4/3}} \frac{(GM_c)^{5/3}}{c^3 D_L^2} \frac{1}{f_{\text{orb}}^{1/3}} \frac{g(n,e)}{nF(e)}, \quad (11)$$

where D_L is the luminosity distance to the source, f_{orb} is the orbital frequency, $g(n,e)$ and $F(e)$ are given in

Peters & Mathews (1963) and \mathcal{M}_c is the chirp mass, defined as

$$\mathcal{M}_c = \frac{(m_1 m_2)^{3/5}}{(m_1 + m_2)^{1/5}}. \quad (12)$$

We use LEGWORK to calculate the signal-to-noise ratio for each binary and the package ensures that enough harmonics are computed for each binary such that the error on the gravitational wave luminosity remains below 1%.

2.3.3. Detection rate calculation

For each physics variation model, we compute the total number of merging DCOs in the Milky Way today based on the COMPAS simulation. This takes into account the true mass and IMF of the Milky Way since our simulations each have a slightly smaller galaxy size and only sample from massive stars rather than the full IMF. For a more in-depth discussion of this process see Appendix A.

We determine the fraction of binaries that are detectable in each Milky Way instance by summing the adaptive importance sampling weights of the binaries that have an SNR greater than 7 and dividing by the total weights in the simulation. We multiply this fraction by the total number in the Milky Way to find a detection rate.

$$N_{\text{detect}} = \frac{\sum_{i=0}^{N_{\text{detect}}} w_i}{\sum_{i=0}^{N_{\text{DCO}}} w_i} \cdot N_{\text{MW}} \quad (13)$$

We calculate this detection rate by Monte Carlo sampling 2500 Milky Way instances (each containing 100,000 DCOs) for each DCO type and every physics variation in order to obtain values for the uncertainty on the expected detection rate.

3. RESULTS

In this section we present our main results for the detectable LISA DCO population. We first show the distribution of the sources on the sensitivity curve before exploring the variations in the detection rate over different physics variations and analysing the parameter distributions for detectable sources in the fiducial model.

3.1. Distribution on the sensitivity curve

We illustrate the distribution of detectable DCOs on the sensitivity curve in Figure 2. In addition to the density distributions we plot grid lines of constant distance and inspiral time to explain the shape of the distribution. The straight diagonal lines show where a binary at a fixed distance would lie on the sensitivity curve for different frequencies and the average chirp mass (annotated in each panel). We would therefore expect that if

a population was entirely circular, it should be bounded approximately between the 0.1–30 kpc lines (roughly the minimum and maximum distance to a source in the Milky Way). If we focus on the bottom panels with each individual DCO type, we see that, though this is the true for a large fraction of the population, there is a distinct subpopulation of binaries that extend downwards around 2×10^{-3} Hz. This offshoot is composed of eccentric binaries for which the circular distance contours will not apply. We therefore also plot a line of constant distance at 30 kpc for an eccentric binary with $e = 0.97$ to show the differences for eccentric sources. We also note that the peak of the density distribution coincides with the centre of the Milky Way as expected, since binaries are most likely to be formed towards the centre of the Galaxy.

We also plot vertical lines that give the inspiral time for a circular binary with the average chirp mass (annotated in each panel). From these lines, it is clear why the density distribution decreases with increasing frequency, since high frequencies correspond to short inspiral times and thus DCOs will spend less time in these regimes. We also see that the tail of the high frequency sources is more numerous near to the Galactic centre than at short distances. This is simply because there are more sources in the galactic centre and so the chances of ‘catching’ a binary at high frequency is better.

3.2. Detection rates

We find that on average, for our fiducial model, a four year LISA mission will detect $25.9_{-11.1}^{+13.6}$ BHBHs, $26.7_{-11.9}^{+14.8}$ BHNSs and $11.3_{-6.4}^{+8.0}$ NSNSs where the error bars represent the 90% confidence interval. Increasing the LISA mission length to ten years changes the number of detections to $42.0_{-17.3}^{+17.3}$, $44.5_{-17.8}^{+20.7}$ and $19.3_{-8.0}^{+9.7}$ respectively. In Figure 3, we show the expected number of LISA detections for each model variation and discuss the prominent trends in the following sections. We show the rates and uncertainties plotted in this figure in Table 2.

3.2.1. BHBH detection rate trends

The BHBH detection rate is markedly robust across physics variations, with the expected detections in each model staying within 25% of the fiducial rate (with the exception of model H). Thus even if there are changes in our understanding of the underlying physics before the LISA mission commences, the expected BHBH detection rate is unlikely to change significantly.

The exception to this statement is model H, in which we allow Hertzsprung gap donors to survive common envelope events. A large fraction of the progenitors of BHs in this mass range expand significantly during

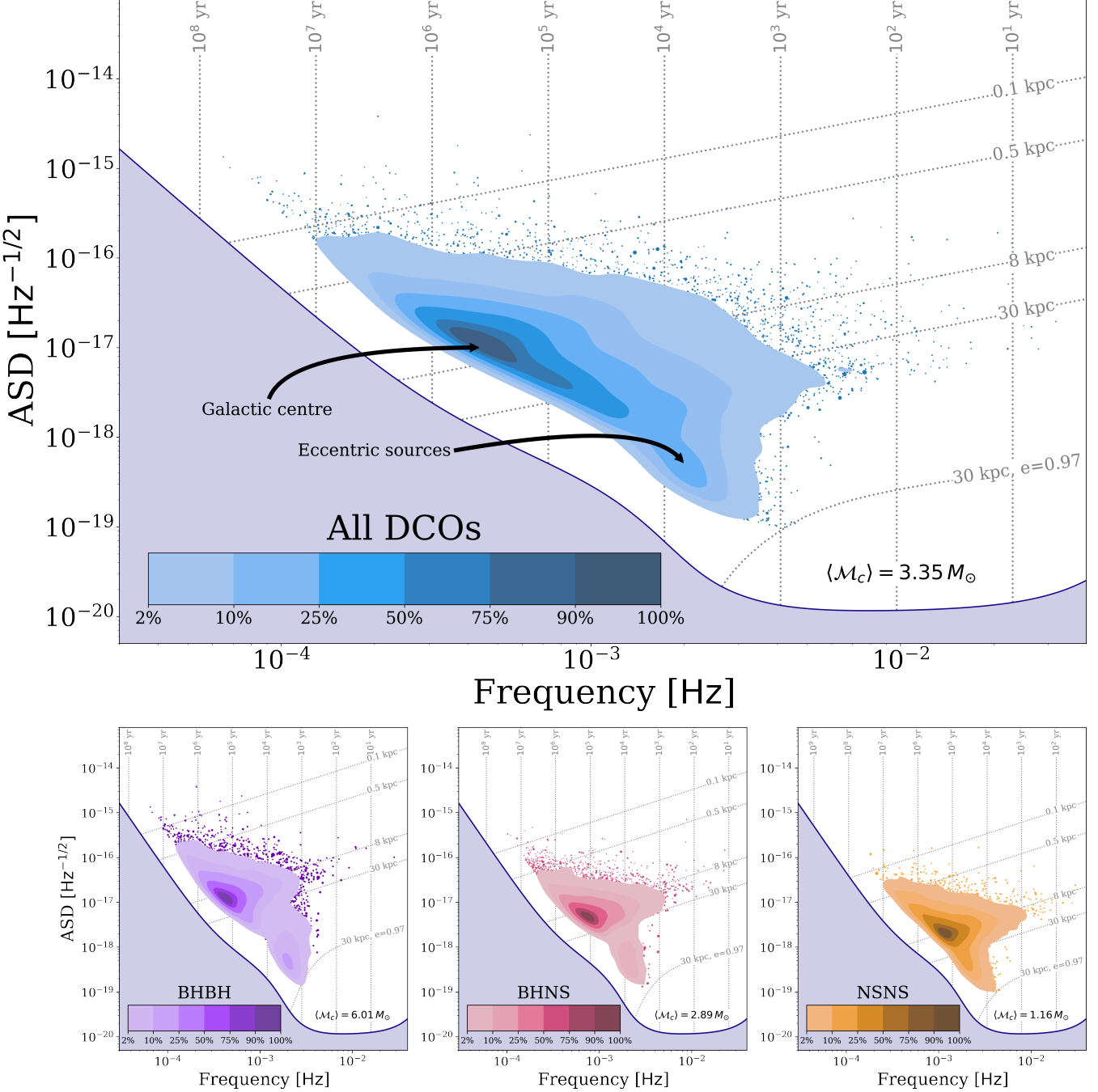


Figure 2. Density distribution of detectable DCOs plotted over the LISA sensitivity curve, where the panels correspond to **top**: combined density plot for all DCO types (BHBH, BHNS and NSNS) **bottom**: three panels with individual density distribution of different DCO types. In each panel, we plot the total signal of binaries at their dominant frequency $n f_{\text{orb}}$, such that n is the harmonic that produces the most relative gravitational wave luminosity ($n = 2$ for circular binaries). If the density of points is below our lowest contour (2%) then we plot the points as scatter points, where their sizes corresponds to their STROOPWAFEL weights. The inset colourbars indicate the percentage of the population represented by each contour and the annotated mass is the average chirp mass for all binaries in the panel, which is used in plotting the grid lines. We plot diagonal lines of constant distance, where the straight lines show the signal for a circular binary of average chirp mass, whilst the dashed line shows the signal for an eccentric binary with $e = 0.97$. The vertical lines indicate the inspiral time for a circular binary with the average chirp mass.

the Hertzsprung gap phase and initiate common envelope events. Therefore, though the detectable fraction does not change significantly, the increased population of BHBHs in the Milky Way leads to this model predicting 2.5 times more detections.

3.2.2. BHNS detection rate trends

In contrast, the BHNS detection rate is very sensitive to changes in binary physics assumptions. Therefore, once LISA flies and we know the actual number of detections, we can compare to each model and possibly provide some constraint on binary evolution physics. There are several notable trends in the BHNS detection rate in the middle pane of Figure 3.

As β increases in models B-D, the BHNS detection rate steadily decreases. This may seem unintuitive since a higher mass transfer efficiency should lead to more massive compact objects and thus a more detectable population. However, one must also consider that most of these DCOs are formed through a common envelope event and so retaining more of the envelope during mass transfer means that the eventual ejection of the envelope is much more difficult, thus leading to more stellar mergers and fewer detectable BHNSs (e.g. Kruckow et al. 2018).

[Tom: @Selma, the trend with common envelopes still confuses me, specifically, why does it not increase when $\alpha = 2.0$? We never quite resolved this in the thread in zpro_tom_wagg with me and Lieke. I do see that the BHBH have a lot of only stable mass transfer and so reasonably are not too affected. NSNS basically only come through CE events and so sensibly are strongly affected but BHNS have $\sim 70\%$ classic channel and so should be affected strongly. But we don't see an increase with $\alpha = 2.0$. Any thoughts?]

Enforcing that case BB mass transfer is always unstable (model E) decreases the detection rate as fewer NSs are produced and thus fewer BHNSs form. This is explained in further detail in Section 3.2.3. For the same reason as the BHBH rate, model H has a higher number of detections. This change is less prominent than in the BHBH case as the progenitors tend to be lower masses and initiate a CE event less frequently during the Hertzsprung gap phase.

The Fryer *rapid* prescription (model I) leads to a higher detection rate for BHNSs because progenitors that would become black holes in the *delayed* prescription, instead become neutron stars and so more BHNSs are formed instead of BHBHs. For the same reason, increasing the maximum neutron star mass (model K) increases the detection rate and the inverse is true when it is decreased (model J).

Finally, models M-O show increased detection rates since lower kicks result in fewer disrupted binaries and hence a more numerous detectable population. Following this logic it makes sense that model N produces more detections than model M. The model with no BH kick (O) is slightly lower than model N as the number of surviving binaries is limited by the neutron star kick more than the black hole kick.

3.2.3. NSNS detection rate trends

As β increases the NSNS detection rate increases, the opposite trend to that seen in the BHNS rate. This is for two main reasons: firstly the ejection of a common envelope is less problematic for the less massive NSNS binaries. Moreover, the increased mass transfer efficiency means that systems that were previously below the mass necessary to become a NS can now accrete enough mass to form a NS. Although the same is true for more massive stars becoming BHs instead of NSs, due to the IMF, there is a net flux of more stars becoming NSs.

There is a drastic decrease in detections for model E by nearly two orders of magnitude. This is because the majority of NSNS binaries are formed through case BB mass transfer and setting this mass transfer to be always unstable results in many of these binaries to merge before they could become NSNSs. As a result the total number of detections decreases, however, interestingly the remaining population represent more massive progenitors (that would not go through case BB mass transfer) and thus is skewed to higher masses and has a *higher* detectable fraction (see Fig. 10).

The vast majority of NSNSs in our sample are formed through the common envelope channel and thus changing the value of α_{CE} has an effect on the rate. We see that decreasing α_{CE} (model F) leads to a lower rate as there is less energy available to eject the envelope and so more binaries result to stellar mergers rather than NSNSs and similarly we see an inverse trend when increasing α_{CE} (model G).

As we found in the BHNS trends, a lower value for the core-collapse supernova velocity dispersion increases the detection rate in models M and N, whilst changing the PISN or BH kick prescription (models L and O) of course has no effect on the NSNS population.

3.3. Distributions for the fiducial model

In Figure 4, we show the distribution of the individual parameters of the population of detectable binaries and discuss the various features in the following sections.

3.3.1. Black Hole Mass

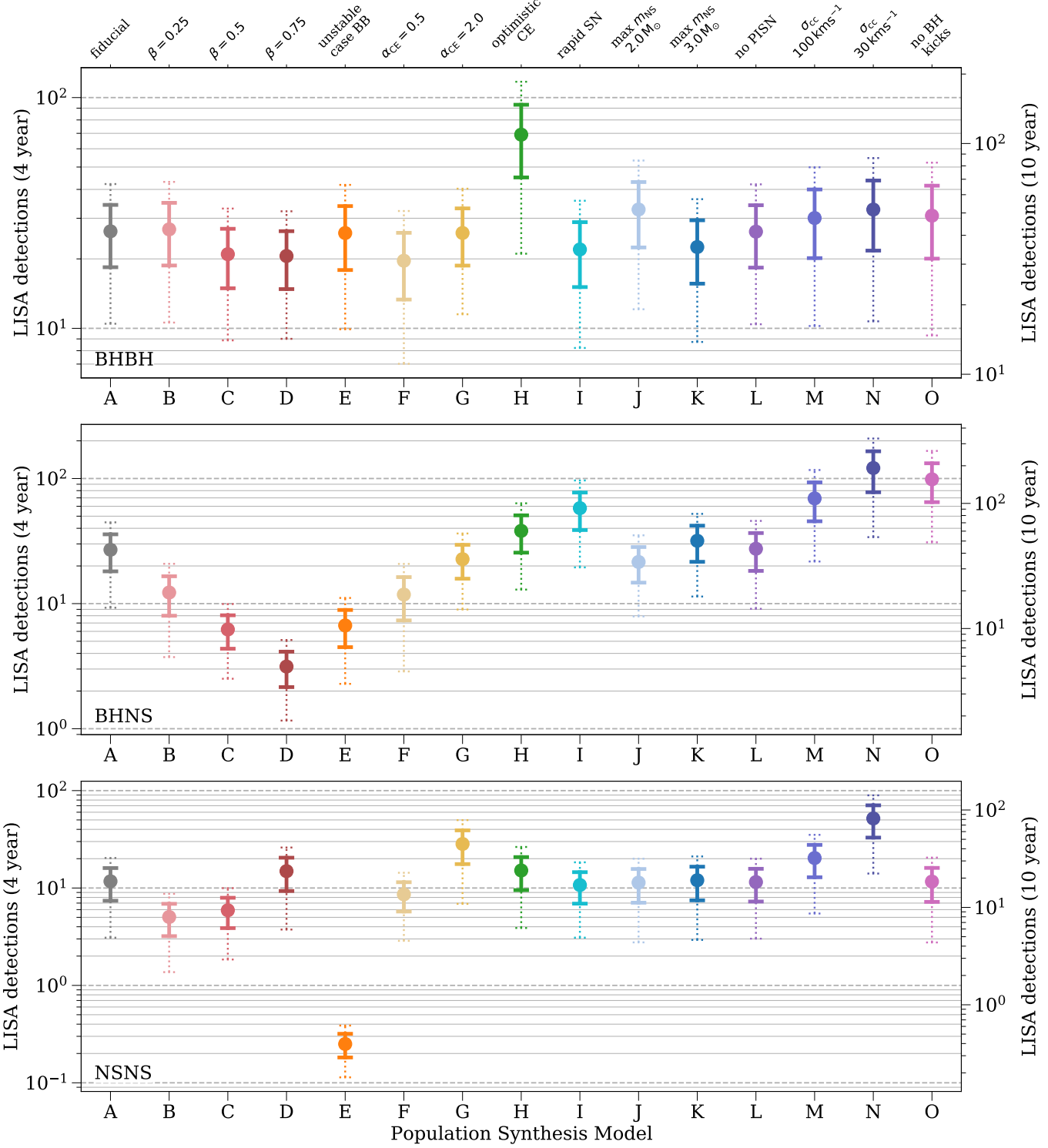


Figure 3. The number of expected detections in the LISA mission for different DCO types and model variations. Error bars show the 1 (solid) and 2 (dotted) σ uncertainties. The left axis and grid lines show the number of detections in a four year LISA mission and the right axis shows an approximation of the number of detections in a 10 year mission (we scale the axis by $\sqrt{T_{\text{obs}}}$, see Table 2 for exact rates). Each model is described in further detail in Table 1 and details of the fiducial assumptions are in Section 2.1.3

For both the BHBHs and BHNSs, the black hole mass distribution extends across relatively low masses, with 83% and 90% respectively below $10 M_{\odot}$. This is because, at the high metallicities in the Milky Way, stellar winds are much stronger and strip away much of the stellar mass before BH formation. The mass distribution also extends down to $2.5 M_{\odot}$, our fiducial maximum neutron star mass, since the Fryer et al. (2012) *delayed* remnant mass prescription does not produce a mass gap between neutron stars and black holes. Thus BHBHs and BHNSs detected by LISA could be ideal for ascertaining whether there exists a lower mass gap between neutron stars and black holes.

The bimodality of the BHBH distribution is a result of most detectable BHBHs in our sample having unequal mass ratios. The two peaks are from the primary and secondary black hole masses and we show their individual distributions with the dotted curves.

The reasoning for these unequal mass ratio is as follows: in order to produce a BHBH, most formation channels require at least the first mass transfer to be stable. This stability is strongly dependent on the mass ratio such that equal mass ratios (at the moment of mass transfer) are preferred for creating BHBHs. Yet, since stellar winds are so strong at high metallicity, and even stronger for more massive stars, the primary star will experience significant mass loss and so an initially *unequal* mass ratio is preferred so that the masses are more balanced at the first instance of mass transfer. Since mass transfer occurs after the end of the main sequence for most of our BHBHs, the star will have a well defined core and these core masses, which go on to form BHs, will reflect the initially unequal mass ratios.

3.3.2. Neutron Star Mass

The neutron star mass distribution shows that most neutron stars have low masses, with 69% and 87% having masses below $1.5 M_{\odot}$ for BHNSs and NSNSs respectively. The lacks of neutron stars around $1.7 M_{\odot}$ and the subsequent small peaks are artifacts of the discontinuous nature of the Fryer et al. (2012) remnant mass prescription.

3.3.3. Eccentricity

The eccentricity distributions show that detectable BHBHs are the most eccentric of the three DCOs. This may seem counter-intuitive since neutron stars receive stronger natal kicks, which cause the orbit to become eccentric. However, these stronger kicks often instead result in disrupted or too-wide binaries. In contrast, BHBHs can receive strong kicks that impart high eccentricity without disrupting and thus tend to be more eccentric. This effect is compounded by the fact that

we can see BHBHs at lower orbital frequencies, meaning that they have not had as much time to circularise and so still have significant eccentricity by the time of the LISA mission.

3.3.4. Orbital Frequency and Frequency Evolution

The orbital frequency distributions for BHBHs, BHNSs and NSNSs peak at increasing frequencies. This is because a higher mass DCO at the same distance and eccentricity requires a lower frequency to produce the same signal-to-noise ratio and thus be detected. The BHBH distribution also has a tail that extends to 4×10^{-6} Hz, which is comprised of highly eccentric binaries since eccentricity moves the dominant harmonic to higher frequencies. Similar tails are not as prevalent for BHNSs and NSNSs as they do not have as many eccentric binaries.

3.3.5. Luminosity Distance

Each DCO's luminosity distance distribution peaks around 8 kpc since this is the distance to the centre of the Milky Way and thus the most dense location of DCOs. Each DCO also has a shoulder at lower distances since closer binaries are easier to detect. This shoulder is more prominent for the NSNS distribution since their lower relative masses require a smaller distance in order to be detected on average.

3.3.6. Inspiral Time

Each DCO has a strong peak at small inspiral times since higher metallicities lead to tighter binaries and thus shorter inspiral times. [TODO: explain the bumps]

3.4. Distinguishing DCOs

[TODO:]

3.5. Model variations

4. DISCUSSION

4.1. Caveats

- Standard pop synth limitations
- Systemic kicks
- No models for high Z values in Frankel
- Only a single disc for the Milky Way

4.2. Can we distinguish them?

5. COMPARISON WITH PREVIOUS STUDIES

[TODO: In this section I will discuss the information in the Figure 5]

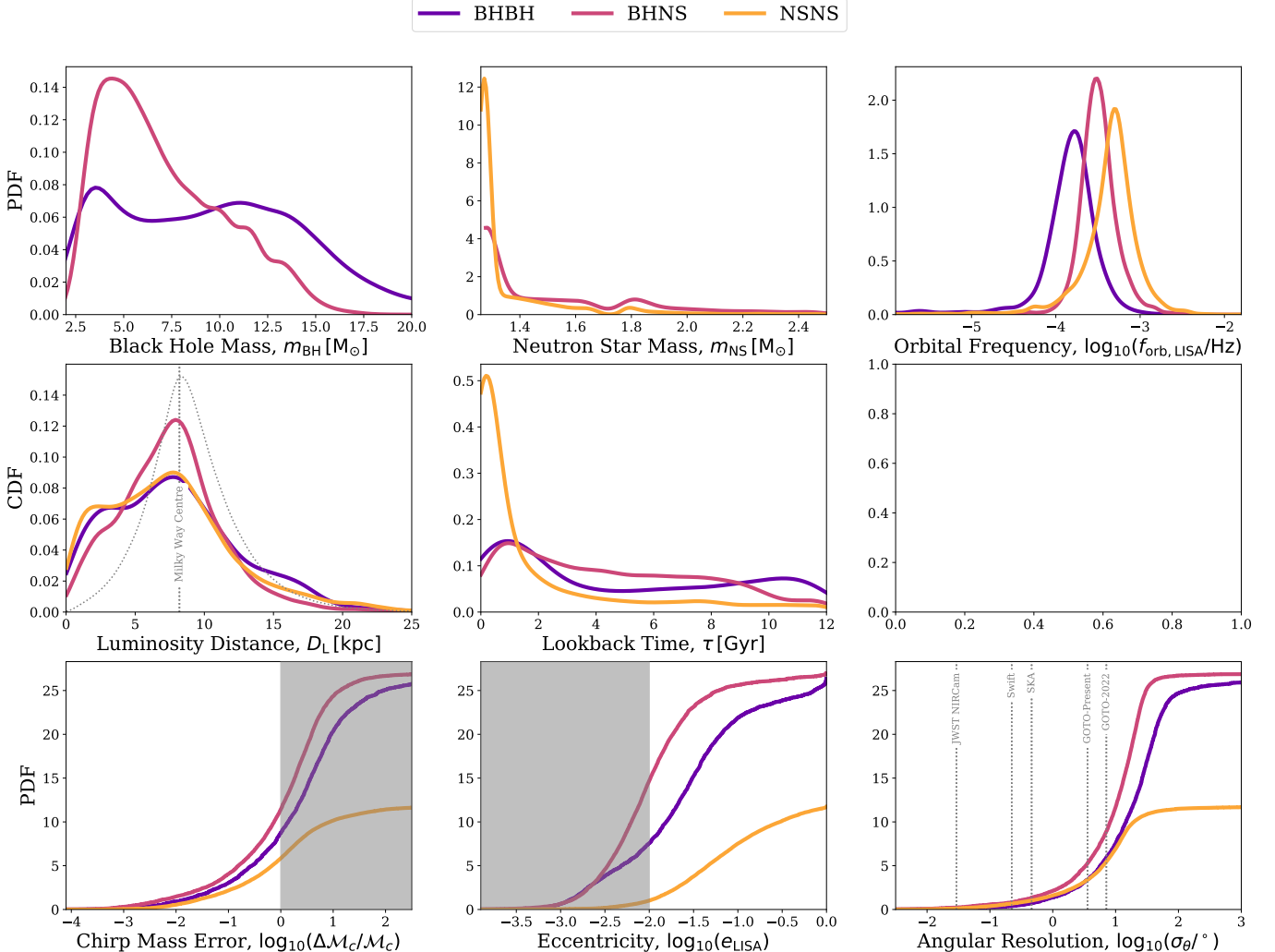


Figure 4. Distributions for various parameters of the binaries that are detectable in a 4 year LISA mission in our fiducial model. Each line represents a kernel density estimator for the distribution and the colour denotes the double compact object type. The dotted curves in the black hole mass distribution show the primary and secondary mass distributions. In Section 3.3 we the features of the distributions.

6. CONCLUSION & SUMMARY

Software: COMPAS (version 02.12.00) <http://github.com/TeamCOMPAS/COMPAS>. (Stevenson et al. 2017; Vigna-Gómez et al. 2018; Broekgaarden et al. 2019), Python available from python.org, matplotlib (Hunter 2007), NumPy (van der Walt et al. 2011), Astropy (<http://www.astropy.org> Astropy Collaboration et al. 2013, 2018).

ACKNOWLEDGMENTS

This project was funded in part by the European Union’s Horizon 2020 research and innovation program from the European Research Council (ERC, Grant agreement No. 715063), and by the Netherlands Organization for Scientific Research (NWO) as part of the Vidi research program BinWaves with project number 639.042.728. We further acknowledge the Black Hole Initiative funded by a generous contribution of the John Templeton Foundation and the Gordon and Betty Moore Foundation.

Author	Year	DCO Predictions			Galaxy and Positioning				
		BHBH	BHNS	NSNS	Star formation history	Spatial distribution		Galactic Components	Metallicity Dependent Distributions
Wagg	2021	25.9, 42.0	26.7, 44.5	11.3, 19.3	Exponential, radially dependent	Frankel+2018 radial, McMillan 2011 vertical (disc)	Thin disc	✓	
Sesana	2020	4.2, 6.5	X	X	FIRE simulation	FIRE simulation	Everything within 300kpc	✓	
Breivik	2020	93	33	8	Constant over 10 Gyr (thin disc), 1 Gyr burst 10 Gyr ago (bulge), 1 Gyr burst 11 Gyr (thick disc)	McMillan 2011	Disc (thin + thick), bulge	X	
Lau	2020	X	X	35	Constant	Miyamoto+Nagai potential (disc); Wilkinson & Evans potential (halo)	Disc or halo	X	
Lamberts	2018	25	X	X	FIRE simulation	FIRE simulation	Everything within 300kpc	✓	
Liu	2014	6	3	16	Constant over 13.7 Gyr	Exponential radial, sech vertical (Eq.13 based on Benacquista+2007)	Disc	X	
Belczynski	2010	2.3, 0	0.2, 0	4, 1.7	Constant over 10 Gyr (disc), 1 Gyr burst 10 Gyr ago (bulge), burst at 13 Gyr (halo)	Exponential sphere (bulge), exponential radial and vertical (disc), spherical shell (halo)	Disc, bulge, halo	X	
Nelemans	2001	0	3	39	Exponential (Eq. 4)	Exponential radial, sech vertical (Eq. 5)	Disc	X	

Author	Year	Population Synthesis				Detection		
		Code	Metallicity	Binary Physics Variations	SNR Limit	LISA Mission Time (years)	Eccentricity Treatment	
Wagg	2021	COMPAS	50 bins between [1e-4, 3e-2]	15	7	4, 10	Full	
Sesana	2020	BSE	13 bins between [1e-4, 3e-2]	None	7	4, 10	Used for evolution, ignored during detection	
Breivik	2020	COSMIC	0.02, 0.003	None	7	4	Full	
Lau	2020	COMPAS	0.0142	Case BB always unstable, Single SN, alpha=0.1	8	4	Full	
Lamberts	2018	BSE	13 bins between [1e-4, 3e-2]	None	5	4	Used for evolution, ignored during detection	
Liu	2014	BSE	0.02	None	7	2	Assumed circular	
Belczynski	2010	Startrack	0.02 (disc, bulge), 0.001 (halo)	Optimistic CE, Pessimistic CE	10	1	Full	
Nelemans	2001	SeBa	0.02	None	1, 5	1	Full	

Figure 5. A table comparing previous studies of a similar nature to this work. The works listed in the table are Nelemans et al. (2001); Belczynski et al. (2010); Liu & Zhang (2014); Lamberts et al. (2018); Lau et al. (2020); Breivik et al. (2020); Sesana et al. (2020).

REFERENCES

- Abbott, B. P., Abbott, R., Abbott, T. D., et al. 2016, Physical Review X, 6, 041015, doi: [10.1103/PhysRevX.6.041015](https://doi.org/10.1103/PhysRevX.6.041015)
- . 2019, Physical Review X, 9, 031040, doi: [10.1103/PhysRevX.9.031040](https://doi.org/10.1103/PhysRevX.9.031040)
- . 2020a, ApJL, 892, L3, doi: [10.3847/2041-8213/ab75f5](https://doi.org/10.3847/2041-8213/ab75f5)
- . 2017, PhRvL, 119, 161101, doi: [10.1103/PhysRevLett.119.161101](https://doi.org/10.1103/PhysRevLett.119.161101)
- Abbott, R., Abbott, T. D., Abraham, S., et al. 2020b, arXiv e-prints, arXiv:2010.14527. <https://arxiv.org/abs/2010.14527>
- . 2020c, ApJL, 896, L44, doi: [10.3847/2041-8213/ab960f](https://doi.org/10.3847/2041-8213/ab960f)
- Abt, H. A. 1983, ARA&A, 21, 343, doi: [10.1146/annurev.aa.21.090183.002015](https://doi.org/10.1146/annurev.aa.21.090183.002015)
- Amaro-Seoane, P., Audley, H., Babak, S., et al. 2017, arXiv e-prints, arXiv:1702.00786. <https://arxiv.org/abs/1702.00786>
- Astropy Collaboration, Price-Whelan, A. M., Sipőcz, B. M., et al. 2018, AJ, 156, 123, doi: [10.3847/1538-3881/aabc4f](https://doi.org/10.3847/1538-3881/aabc4f)
- Astropy Collaboration, Robitaille, T. P., Tollerud, E. J., et al. 2013, A&A, 558, A33, doi: [10.1051/0004-6361/201322068](https://doi.org/10.1051/0004-6361/201322068)
- Barack, L., & Cutler, C. 2004, PhRvD, 69, 082005, doi: [10.1103/PhysRevD.69.082005](https://doi.org/10.1103/PhysRevD.69.082005)
- Baxter, E. J., Croon, D., McDermott, S. D., & Sakstein, J. 2021, arXiv e-prints, arXiv:2104.02685. <https://arxiv.org/abs/2104.02685>
- Belczynski, K., Benacquista, M., & Bulik, T. 2010, ApJ, 725, 816, doi: [10.1088/0004-637X/725/1/816](https://doi.org/10.1088/0004-637X/725/1/816)
- Belczynski, K., Taam, R. E., Kalogera, V., Rasio, F. A., & Bulik, T. 2007, ApJ, 662, 504, doi: [10.1086/513562](https://doi.org/10.1086/513562)
- Bertelli, G., Bressan, A., Chiosi, C., Fagotto, F., & Nasi, E. 1994, A&AS, 106, 275
- Blaauw, A. 1961, BAN, 15, 265
- Breivik, K., Coughlin, S., Zevin, M., et al. 2020, ApJ, 898, 71, doi: [10.3847/1538-4357/ab9d85](https://doi.org/10.3847/1538-4357/ab9d85)
- Breivik, K., Rodriguez, C. L., Larson, S. L., Kalogera, V., & Rasio, F. A. 2016, ApJL, 830, L18, doi: [10.3847/2041-8205/830/1/L18](https://doi.org/10.3847/2041-8205/830/1/L18)
- Broekgaarden, F. S., Berger, E., Neijssel, C. J., et al. 2021, arXiv e-prints, arXiv:2103.02608. <https://arxiv.org/abs/2103.02608>
- Broekgaarden, F. S., Justham, S., de Mink, S. E., et al. 2019, MNRAS, 490, 5228, doi: [10.1093/mnras/stz2558](https://doi.org/10.1093/mnras/stz2558)
- Chattopadhyay, D., Stevenson, S., Hurley, J. R., Bailes, M., & Broekgaarden, F. 2020, arXiv e-prints, arXiv:2011.13503. <https://arxiv.org/abs/2011.13503>
- de Kool, M. 1990, ApJ, 358, 189, doi: [10.1086/168974](https://doi.org/10.1086/168974)
- de Mink, S. E., & Belczynski, K. 2015, ApJ, 814, 58, doi: [10.1088/0004-637X/814/1/58](https://doi.org/10.1088/0004-637X/814/1/58)
- Eichler, D., Livio, M., Piran, T., & Schramm, D. N. 1989, Nature, 340, 126, doi: [10.1038/340126a0](https://doi.org/10.1038/340126a0)
- Farmer, R., Renzo, M., de Mink, S. E., Marchant, P., & Justham, S. 2019, ApJ, 887, 53, doi: [10.3847/1538-4357/ab518b](https://doi.org/10.3847/1538-4357/ab518b)
- Finn, L. S., & Thorne, K. S. 2000, PhRvD, 62, 124021, doi: [10.1103/PhysRevD.62.124021](https://doi.org/10.1103/PhysRevD.62.124021)
- Frankel, N., Rix, H.-W., Ting, Y.-S., Ness, M., & Hogg, D. W. 2018, ApJ, 865, 96, doi: [10.3847/1538-4357/aadba5](https://doi.org/10.3847/1538-4357/aadba5)
- Fryer, C. L., Belczynski, K., Ramirez-Ruiz, E., et al. 2015, ApJ, 812, 24, doi: [10.1088/0004-637X/812/1/24](https://doi.org/10.1088/0004-637X/812/1/24)
- Fryer, C. L., Belczynski, K., Wiktorowicz, G., et al. 2012, ApJ, 749, 91, doi: [10.1088/0004-637X/749/1/91](https://doi.org/10.1088/0004-637X/749/1/91)
- Gaia Collaboration, Prusti, T., de Bruijne, J. H. J., et al. 2016, A&A, 595, A1, doi: [10.1051/0004-6361/201629272](https://doi.org/10.1051/0004-6361/201629272)
- Gerosa, D., Ma, S., Wong, K. W. K., et al. 2019, PhRvD, 99, 103004, doi: [10.1103/PhysRevD.99.103004](https://doi.org/10.1103/PhysRevD.99.103004)
- Gompertz, B. P., Levan, A. J., & Tanvir, N. R. 2020, ApJ, 895, 58, doi: [10.3847/1538-4357/ab8d24](https://doi.org/10.3847/1538-4357/ab8d24)
- Hjellming, M. S., & Webbink, R. F. 1987, ApJ, 318, 794, doi: [10.1086/165412](https://doi.org/10.1086/165412)
- Hobbs, G., Lorimer, D. R., Lyne, A. G., & Kramer, M. 2005, MNRAS, 360, 974, doi: [10.1111/j.1365-2966.2005.09087.x](https://doi.org/10.1111/j.1365-2966.2005.09087.x)
- Hotokezaka, K., Nissanke, S., Hallinan, G., et al. 2016, ApJ, 831, 190, doi: [10.3847/0004-637X/831/2/190](https://doi.org/10.3847/0004-637X/831/2/190)
- Hulse, R. A., & Taylor, J. H. 1975, ApJL, 195, L51, doi: [10.1086/181708](https://doi.org/10.1086/181708)
- Hunter, J. D. 2007, Computing in Science and Engineering, 9, 90, doi: [10.1109/MCSE.2007.55](https://doi.org/10.1109/MCSE.2007.55)
- Hurley, J. R., Pols, O. R., & Tout, C. A. 2000, MNRAS, 315, 543, doi: [10.1046/j.1365-8711.2000.03426.x](https://doi.org/10.1046/j.1365-8711.2000.03426.x)
- Hurley, J. R., Tout, C. A., & Pols, O. R. 2002, MNRAS, 329, 897, doi: [10.1046/j.1365-8711.2002.05038.x](https://doi.org/10.1046/j.1365-8711.2002.05038.x)
- Ianova, N., Heinke, C. O., Rasio, F. A., Belczynski, K., & Fregeau, J. M. 2008, MNRAS, 386, 553, doi: [10.1111/j.1365-2966.2008.13064.x](https://doi.org/10.1111/j.1365-2966.2008.13064.x)
- Ianova, N., & Taam, R. E. 2004, ApJ, 601, 1058, doi: [10.1086/380561](https://doi.org/10.1086/380561)
- Kalogera, V., & Baym, G. 1996, ApJL, 470, L61, doi: [10.1086/310296](https://doi.org/10.1086/310296)
- Korol, V., Rossi, E. M., Groot, P. J., et al. 2017, MNRAS, 470, 1894, doi: [10.1093/mnras/stx1285](https://doi.org/10.1093/mnras/stx1285)
- Korol, V., Toonen, S., Klein, A., et al. 2020, A&A, 638, A153, doi: [10.1051/0004-6361/202037764](https://doi.org/10.1051/0004-6361/202037764)

- Kroupa, P. 2001, MNRAS, 322, 231, doi: [10.1046/j.1365-8711.2001.04022.x](https://doi.org/10.1046/j.1365-8711.2001.04022.x)
- Kruckow, M. U., Tauris, T. M., Langer, N., Kramer, M., & Izzard, R. G. 2018, MNRAS, 481, 1908, doi: [10.1093/mnras/sty2190](https://doi.org/10.1093/mnras/sty2190)
- Kyutoku, K., Kiuchi, K., Sekiguchi, Y., Shibata, M., & Taniguchi, K. 2018, PhRvD, 97, 023009, doi: [10.1103/PhysRevD.97.023009](https://doi.org/10.1103/PhysRevD.97.023009)
- Lamberts, A., Blunt, S., Littenberg, T. B., et al. 2019, MNRAS, 490, 5888, doi: [10.1093/mnras/stz2834](https://doi.org/10.1093/mnras/stz2834)
- Lamberts, A., Garrison-Kimmel, S., Hopkins, P. F., et al. 2018, MNRAS, 480, 2704, doi: [10.1093/mnras/sty2035](https://doi.org/10.1093/mnras/sty2035)
- Lau, M. Y. M., Mandel, I., Vigna-Gómez, A., et al. 2020, MNRAS, 492, 3061, doi: [10.1093/mnras/staa002](https://doi.org/10.1093/mnras/staa002)
- Licquia, T., & Newman, J. 2014, in American Astronomical Society Meeting Abstracts, Vol. 223, American Astronomical Society Meeting Abstracts #223, 336.04
- Liu, J. 2009, MNRAS, 400, 1850, doi: [10.1111/j.1365-2966.2009.15574.x](https://doi.org/10.1111/j.1365-2966.2009.15574.x)
- Liu, J., & Zhang, Y. 2014, PASP, 126, 211, doi: [10.1086/675721](https://doi.org/10.1086/675721)
- Lyne, A. G., & Lorimer, D. R. 1994, Nature, 369, 127, doi: [10.1038/369127a0](https://doi.org/10.1038/369127a0)
- Majewski, S. R., Schiavon, R. P., Frinchaboy, P. M., et al. 2017, AJ, 154, 94, doi: [10.3847/1538-3881/aa784d](https://doi.org/10.3847/1538-3881/aa784d)
- Marchant, P., Renzo, M., Farmer, R., et al. 2019, ApJ, 882, 36, doi: [10.3847/1538-4357/ab3426](https://doi.org/10.3847/1538-4357/ab3426)
- Margalit, B., & Metzger, B. D. 2017, ApJL, 850, L19, doi: [10.3847/2041-8213/aa991c](https://doi.org/10.3847/2041-8213/aa991c)
- Massevitch, A., & Yungelson, L. 1975, Mem. Soc. Astron. Italiana, 46, 217
- McMillan, P. J. 2011, MNRAS, 414, 2446, doi: [10.1111/j.1365-2966.2011.18564.x](https://doi.org/10.1111/j.1365-2966.2011.18564.x)
- Metzger, B. D. 2017, Living Reviews in Relativity, 20, 3, doi: [10.1007/s41114-017-0006-z](https://doi.org/10.1007/s41114-017-0006-z)
- Nelemans, G., Yungelson, L. R., & Portegies Zwart, S. F. 2001, A&A, 375, 890, doi: [10.1051/0004-6361:20010683](https://doi.org/10.1051/0004-6361:20010683)
- Nissanke, S., Vallisneri, M., Nelemans, G., & Prince, T. A. 2012, ApJ, 758, 131, doi: [10.1088/0004-637X/758/2/131](https://doi.org/10.1088/0004-637X/758/2/131)
- Nomoto, K. 1984, ApJ, 277, 791, doi: [10.1086/161749](https://doi.org/10.1086/161749)
- . 1987, ApJ, 322, 206, doi: [10.1086/165716](https://doi.org/10.1086/165716)
- Öpik, E. 1924, Publications of the Tartu Astrofizika Observatory, 25, 1
- Paczyński, B., & Sienkiewicz, R. 1972, AcA, 22, 73
- Peters, P. C. 1964, Physical Review, 136, 1224, doi: [10.1103/PhysRev.136.B1224](https://doi.org/10.1103/PhysRev.136.B1224)
- Peters, P. C., & Mathews, J. 1963, Physical Review, 131, 435, doi: [10.1103/PhysRev.131.435](https://doi.org/10.1103/PhysRev.131.435)
- Pfahl, E., Rappaport, S., Podsiadlowski, P., & Spruit, H. 2002, ApJ, 574, 364, doi: [10.1086/340794](https://doi.org/10.1086/340794)
- Podsiadlowski, P., Langer, N., Poelarends, A. J. T., et al. 2004, ApJ, 612, 1044, doi: [10.1086/421713](https://doi.org/10.1086/421713)
- Pols, O. R., Schröder, K.-P., Hurley, J. R., Tout, C. A., & Eggleton, P. P. 1998, MNRAS, 298, 525, doi: [10.1046/j.1365-8711.1998.01658.x](https://doi.org/10.1046/j.1365-8711.1998.01658.x)
- Robson, T., Cornish, N. J., & Liu, C. 2019, Classical and Quantum Gravity, 36, 105011, doi: [10.1088/1361-6382/ab1101](https://doi.org/10.1088/1361-6382/ab1101)
- Ruiter, A. J., Belczynski, K., Benacquista, M., Larson, S. L., & Williams, G. 2010, ApJ, 717, 1006, doi: [10.1088/0004-637X/717/2/1006](https://doi.org/10.1088/0004-637X/717/2/1006)
- Sana, H., de Mink, S. E., de Koter, A., et al. 2012, Science, 337, 444, doi: [10.1126/science.1223344](https://doi.org/10.1126/science.1223344)
- Sellwood, J. A., & Binney, J. J. 2002, MNRAS, 336, 785, doi: [10.1046/j.1365-8711.2002.05806.x](https://doi.org/10.1046/j.1365-8711.2002.05806.x)
- Sesana, A., Lamberts, A., & Petiteau, A. 2020, MNRAS, 494, L75, doi: [10.1093/mnrasl/slaa039](https://doi.org/10.1093/mnrasl/slaa039)
- Soberman, G. E., Phinney, E. S., & van den Heuvel, E. P. J. 1997, A&A, 327, 620, <https://arxiv.org/abs/astro-ph/9703016>
- Stevenson, S., Sampson, M., Powell, J., et al. 2019, ApJ, 882, 121, doi: [10.3847/1538-4357/ab3981](https://doi.org/10.3847/1538-4357/ab3981)
- Stevenson, S., Vigna-Gómez, A., Mandel, I., et al. 2017, Nature Communications, 8, 14906, doi: [10.1038/ncomms14906](https://doi.org/10.1038/ncomms14906)
- Taam, R. E., & Sandquist, E. L. 2000, ARA&A, 38, 113, doi: [10.1146/annurev.astro.38.1.113](https://doi.org/10.1146/annurev.astro.38.1.113)
- Tauris, T. M., Langer, N., Moriya, T. J., et al. 2013, ApJL, 778, L23, doi: [10.1088/2041-8205/778/2/L23](https://doi.org/10.1088/2041-8205/778/2/L23)
- Tauris, T. M., Langer, N., & Podsiadlowski, P. 2015, MNRAS, 451, 2123, doi: [10.1093/mnras/stv990](https://doi.org/10.1093/mnras/stv990)
- Timmes, F. X., Woosley, S. E., & Weaver, T. A. 1996, ApJ, 457, 834, doi: [10.1086/176778](https://doi.org/10.1086/176778)
- van der Walt, S., Colbert, S. C., & Varoquaux, G. 2011, Computing in Science and Engineering, 13, 22, doi: [10.1109/MCSE.2011.37](https://doi.org/10.1109/MCSE.2011.37)
- Vigna-Gómez, A., Neijssel, C. J., Stevenson, S., et al. 2018, MNRAS, 481, 4009, doi: [10.1093/mnras/sty2463](https://doi.org/10.1093/mnras/sty2463)
- Webbink, R. F. 1984, ApJ, 277, 355, doi: [10.1086/161701](https://doi.org/10.1086/161701)
- Woosley, S. E., Blinnikov, S., & Heger, A. 2007, Nature, 450, 390, doi: [10.1038/nature06333](https://doi.org/10.1038/nature06333)
- Xu, X.-J., & Li, X.-D. 2010a, ApJ, 716, 114, doi: [10.1088/0004-637X/716/1/114](https://doi.org/10.1088/0004-637X/716/1/114)
- . 2010b, ApJ, 722, 1985, doi: [10.1088/0004-637X/722/2/1985](https://doi.org/10.1088/0004-637X/722/2/1985)
- Yu, S., & Jeffery, C. S. 2010, A&A, 521, A85, doi: [10.1051/0004-6361/201014827](https://doi.org/10.1051/0004-6361/201014827)

APPENDIX

A. DETECTION RATE NORMALISATION

From each instance of the Milky Way that we simulate we can extract the number of targets² that are detectable. However, this number must be normalised in order to show the true detection rate for the Milky Way. Therefore, we write that the number of detectable targets in the Milky Way is

$$N_{\text{detect}} = f_{\text{detect}} \cdot N_{\text{target,MW}}, \quad (\text{A1})$$

where f_{detect} is the fraction of targets in the instance that were detectable and $N_{\text{target,MW}}$ is the total number of targets that have been formed in the Milky Way's history. We can find this total in two steps: (1) find the average number of targets formed per star forming mass (2) find the total star forming mass that has existed in the Milky Way's history.

A.1. Average target formation rate

Since double compact object formation is strongly metallicity dependent, we can find the average rate as the integral over metallicity

$$\langle \mathcal{R}_{\text{target}} \rangle = \int_{Z_{\min}}^{Z_{\max}} p_Z \mathcal{R}_{\text{target},Z} dZ, \quad (\text{A2})$$

where Z_{\min} , Z_{\max} are the minimum and maximum sampled metallicities, p_Z is the probability of forming a star at the metallicity Z (Frankel et al. 2018) and $\mathcal{R}_{\text{target},Z}$ is defined as the number of targets formed per star forming mass.

$$\mathcal{R}_{\text{target},Z} = N_{\text{target},Z} / M_{\text{SF},Z}. \quad (\text{A3})$$

The number of targets in our sample at a metallicity Z can be written simply as the sum of the targets' weights:

$$N_{\text{target},Z} = \sum_{i=1}^{N_{\text{binaries},Z}} w_i \theta_{\text{target},i}, \quad (\text{A4})$$

where w_i is the STROOPWAFEL weight assigned to a binary, $N_{\text{binaries},Z}$ is the number of binaries at metallicity Z in our sample and $\theta_{\text{target},i}$ is a step function that is only 1 when the binary is a target and otherwise 0. The total star forming mass at a metallicity Z can be written as

$$M_{\text{SF},Z} = \frac{\langle m \rangle_{\text{COMPAS},Z}}{f_{\text{trunc}}} \sum_{i=1}^{N_{\text{binaries},Z}} w_i, \quad (\text{A5})$$

where $\langle m \rangle_{\text{COMPAS}}$ is the average star forming mass of a binary in our sample and f_{trunc} is the fraction of the total stellar mass that COMPAS samples from given its truncated mass and separation ranges (see Section 2.1). The cuts applied to the distributions mean that only $f_{\text{trunc}} \approx 0.2$ of the stellar mass is sampled from.

A.2. Total star forming mass in the Milky Way

It is important to distinguish between the *total* star forming mass in the Milky Way and the *current* star forming mass in the Milky Way. Many stars born in the Milky Way are no longer living and have lost much of their mass to stellar winds and supernovae, thus decreasing the total stellar mass. Licquia & Newman (2014) find that the total stellar mass today in the Milky Way disc is $6.08 \pm 1.14 \times 10^{10} \text{ M}_{\odot}$. This total includes all stars and stellar remnants (white dwarfs, neutrons stars and black holes) but *excludes* brown dwarfs. We can write that the total star forming mass that has *ever* existed in the Milky Way is

$$M_{\text{SF,MW}} = 6.08 \pm 1.14 \times 10^{10} \text{ M}_{\odot} \cdot \frac{\langle m \rangle_{\text{SF,total}}}{\langle m \rangle_{\text{SF,today}}}, \quad (\text{A6})$$

²By targets, we are referring to either BHBB, BHNS or NSNS that merge in a Hubble time

where $\langle m \rangle_{\text{SF, total}}$ is the average star forming mass over the history of the Milky Way and $\langle m \rangle_{\text{SF, today}}$ is the average star forming mass of the mass remaining today. The former is defined as

$$\langle m \rangle_{\text{SF, total}} = \int_0^{t_{\text{MW}}} p_{\text{birth}}(t) \int_{0.01}^{200} \zeta(m) m \, dm \, dt, \quad (\text{A7})$$

where t_{MW} is the age of the Milky Way, $\zeta(m)$ is the Kroupa (2001) IMF function and $p_{\text{birth}}(\tau)$ is the probability of a star being formed at a lookback time τ (Frankel et al. 2018, Eq. 4). The average star forming mass of the mass *remaining today* is defined as follows (note that we integrate from 0.08 not 0.01 since observations of today's Milky Way mass exclude brown dwarfs)

$$\langle m \rangle_{\text{SF, today}} = \int_0^{t_{\text{MW}}} p_{\text{birth}}(\tau) \int_{0.08}^{200} \zeta(m) m_{\text{today}}(m, \langle Z \rangle_\tau, \tau) \, dm \, d\tau, \quad (\text{A8})$$

where $m_{\text{today}}(m, Z, \tau)$ is the mass of a star that was formed τ years ago at a metallicity Z . We calculate this by interpolating a grid of single stars in COMPAS over different masses and metallicities and seeing what final mass they get using the Fryer et al. (2012) delayed prescription and default wind mass loss settings. We only use the final mass if more than $\tau_{\text{MS}}(m, Z)$ main sequence lifetime of the star has passed, otherwise we just use the initial mass. Since we don't know the exact metallicity of each star we use the average metallicity in the Milky Way at a lookback time τ using the birth radius distribution and metallicity equation from Frankel et al. (2018). If we now evaluate Equation A6, we find the that total star forming mass that ever existed in the Milky Way is

$$M_{\text{SF, MW}} = 6.1 \pm 1.1 \times 10^{10} M_\odot \cdot \frac{0.384 M_\odot}{0.257 M_\odot} = 9.1 \pm 1.1 \times 10^{10} M_\odot, \quad (\text{A9})$$

an increase of approximately 50% from the value still in stars today.

A.3. Normalisation summary

We can plug Equations A2 and A6 into A1 and write that the overall normalisation of the detection rate is calculated as

$$N_{\text{detect}} = 9.1 \times 10^{10} M_\odot \cdot f_{\text{detect}} \cdot \sum_{Z=Z_{\min}}^{Z_{\max}} p_Z \left(\sum_{i=1}^{N_{\text{binaries}, Z}} w_i \theta_{\text{target}, i} \right) \left(\frac{\langle m \rangle_{\text{COMPAS, Z}}}{f_{\text{trunc}}} \sum_{i=1}^{N_{\text{binaries}, Z}} w_i \right)^{-1} \quad (\text{A10})$$

B. SUPPLEMENTARY MATERIAL

B.1. Detection rate table

B.2. Physics variation cumulative distributions

B.3. Detection rates

B.4. Formation channels

Table 2. The number of detectable binaries in a 4 and 10 year LISA mission for the 15 different model variations and each DCO type. Each value shows the median and the 90% confidence interval.

Model	LISA (4 year)			LISA (10 year)		
	BHBH	BHNS	NSNS	BHBH	BHNS	NSNS
A	$25.9^{+13.6}_{-11.1}$	$26.7^{+14.8}_{-11.9}$	$11.3^{+8.0}_{-6.4}$	$42.0^{+17.3}_{-17.3}$	$44.5^{+20.7}_{-17.8}$	$19.3^{+9.7}_{-8.0}$
B	$27.7^{+12.6}_{-12.6}$	$12.0^{+7.5}_{-6.0}$	$4.7^{+3.3}_{-2.7}$	$42.7^{+17.6}_{-17.6}$	$19.5^{+10.5}_{-7.5}$	$8.0^{+4.0}_{-3.3}$
C	$20.6^{+11.3}_{-9.4}$	$6.2^{+3.4}_{-2.8}$	$5.5^{+4.1}_{-2.7}$	$33.8^{+13.1}_{-13.1}$	$10.1^{+3.9}_{-3.9}$	$9.6^{+4.1}_{-4.1}$
D	$20.0^{+10.0}_{-8.3}$	$3.2^{+1.6}_{-1.6}$	$14.6^{+10.4}_{-8.3}$	$31.7^{+11.7}_{-11.7}$	$5.1^{+2.2}_{-1.9}$	$22.9^{+12.5}_{-10.4}$
E	$24.4^{+14.7}_{-12.2}$	$6.8^{+3.8}_{-3.8}$	$0.2^{+0.1}_{-0.1}$	$41.5^{+17.1}_{-17.1}$	$10.6^{+5.3}_{-3.8}$	$0.4^{+0.2}_{-0.1}$
F	$20.0^{+10.0}_{-10.0}$	$11.5^{+8.2}_{-6.6}$	$8.1^{+5.4}_{-3.6}$	$30.0^{+14.0}_{-12.0}$	$19.7^{+9.9}_{-9.9}$	$13.6^{+6.3}_{-5.4}$
G	$25.7^{+13.8}_{-9.9}$	$23.3^{+10.6}_{-10.6}$	$26.5^{+18.9}_{-15.1}$	$39.5^{+15.8}_{-13.8}$	$36.1^{+17.0}_{-12.7}$	$45.4^{+22.7}_{-18.9}$
H	$63.6^{+47.7}_{-31.8}$	$37.4^{+20.8}_{-20.8}$	$14.7^{+10.5}_{-8.4}$	$103.4^{+55.7}_{-39.8}$	$62.3^{+29.1}_{-24.9}$	$25.2^{+12.6}_{-12.6}$
I	$21.7^{+13.0}_{-10.9}$	$56.8^{+31.6}_{-31.6}$	$11.0^{+6.9}_{-5.5}$	$32.6^{+15.2}_{-13.0}$	$94.7^{+44.2}_{-37.9}$	$17.9^{+8.3}_{-8.3}$
J	$32.6^{+19.6}_{-16.3}$	$20.3^{+13.5}_{-9.0}$	$11.0^{+7.8}_{-6.3}$	$52.2^{+22.8}_{-19.6}$	$33.8^{+15.8}_{-11.3}$	$18.8^{+9.4}_{-7.8}$
K	$21.4^{+11.7}_{-9.7}$	$30.6^{+17.0}_{-13.6}$	$11.5^{+8.2}_{-6.6}$	$35.0^{+15.6}_{-13.6}$	$51.1^{+23.8}_{-20.4}$	$19.8^{+9.9}_{-8.2}$
L	$24.7^{+14.8}_{-9.9}$	$26.7^{+17.8}_{-14.8}$	$11.3^{+8.0}_{-6.4}$	$42.0^{+17.3}_{-14.8}$	$44.5^{+20.7}_{-17.8}$	$19.3^{+9.7}_{-8.0}$
M	$29.7^{+16.5}_{-13.2}$	$70.6^{+39.2}_{-39.2}$	$20.4^{+11.7}_{-11.7}$	$46.1^{+23.1}_{-19.8}$	$109.8^{+54.9}_{-39.2}$	$32.1^{+17.5}_{-14.6}$
N	$31.6^{+19.7}_{-15.8}$	$117.7^{+73.6}_{-58.8}$	$51.8^{+29.6}_{-29.6}$	$51.3^{+23.7}_{-23.7}$	$191.3^{+103.0}_{-73.6}$	$81.4^{+44.4}_{-37.0}$
O	$30.2^{+18.9}_{-15.1}$	$96.7^{+60.4}_{-48.3}$	$11.4^{+8.1}_{-6.5}$	$49.1^{+22.7}_{-22.7}$	$157.1^{+84.6}_{-60.4}$	$19.5^{+9.7}_{-9.7}$

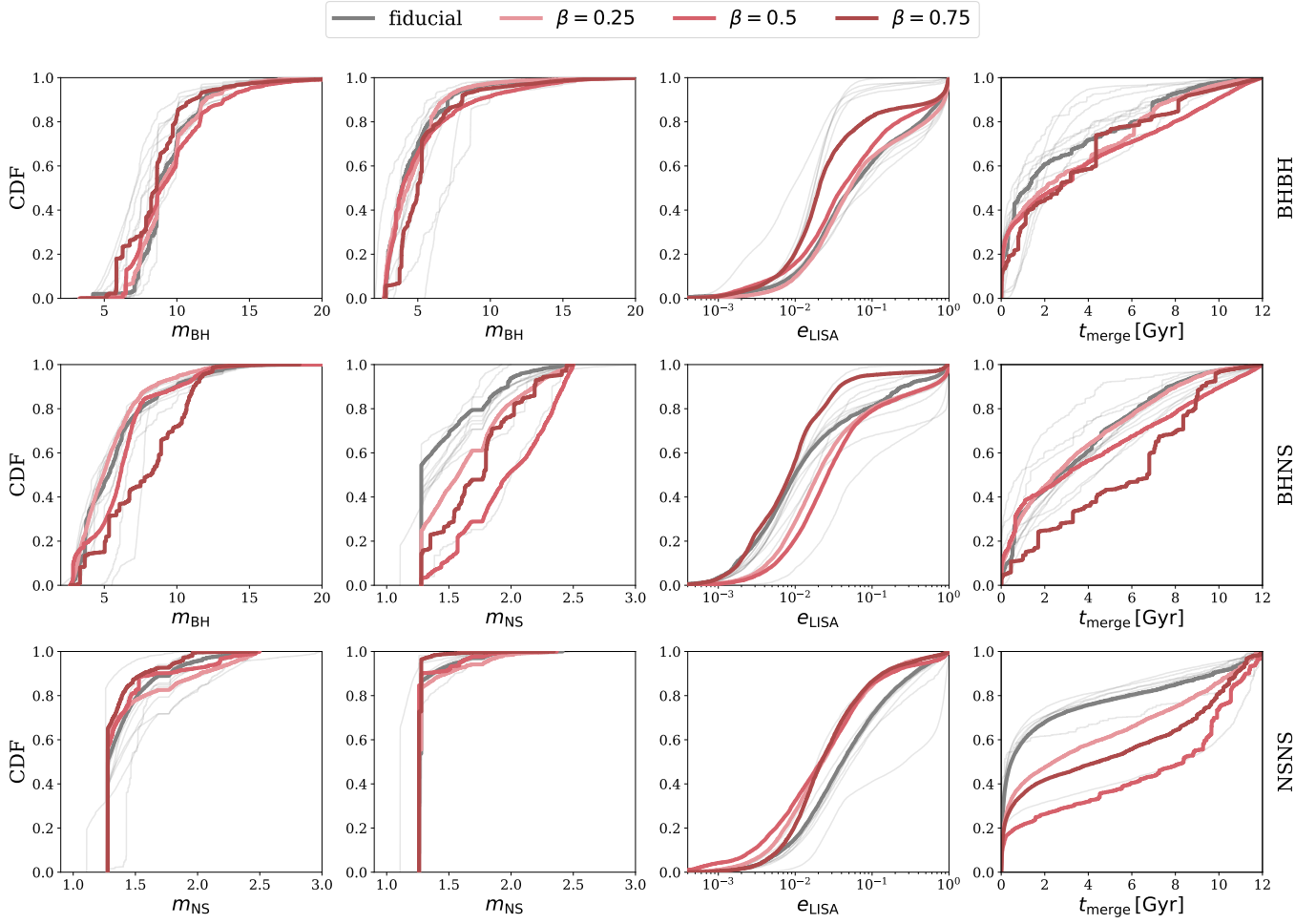


Figure 6. Cumulative distribution functions for the black hole mass, neutron star mass, eccentricity during the LISA mission and merger time for each DCO type and physics variation. In colour we show the fiducial populations compared to changing the mass transfer efficiency β . We additionally show the other physics variations in the background in light grey.

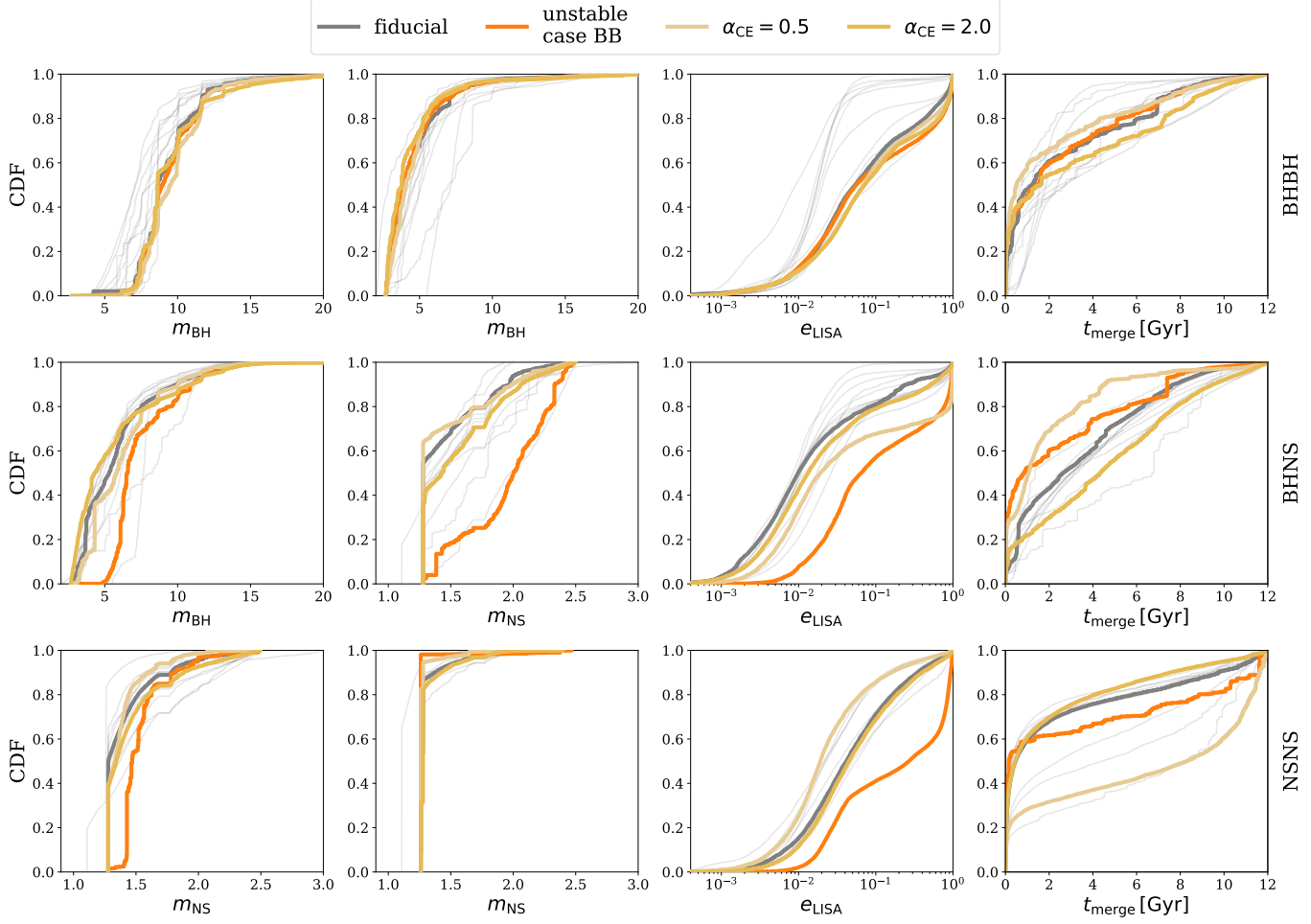


Figure 7. As Fig. 6, except comparing the fiducial population with models using different values for α_{CE} and changing the stability of case BB mass transfer.

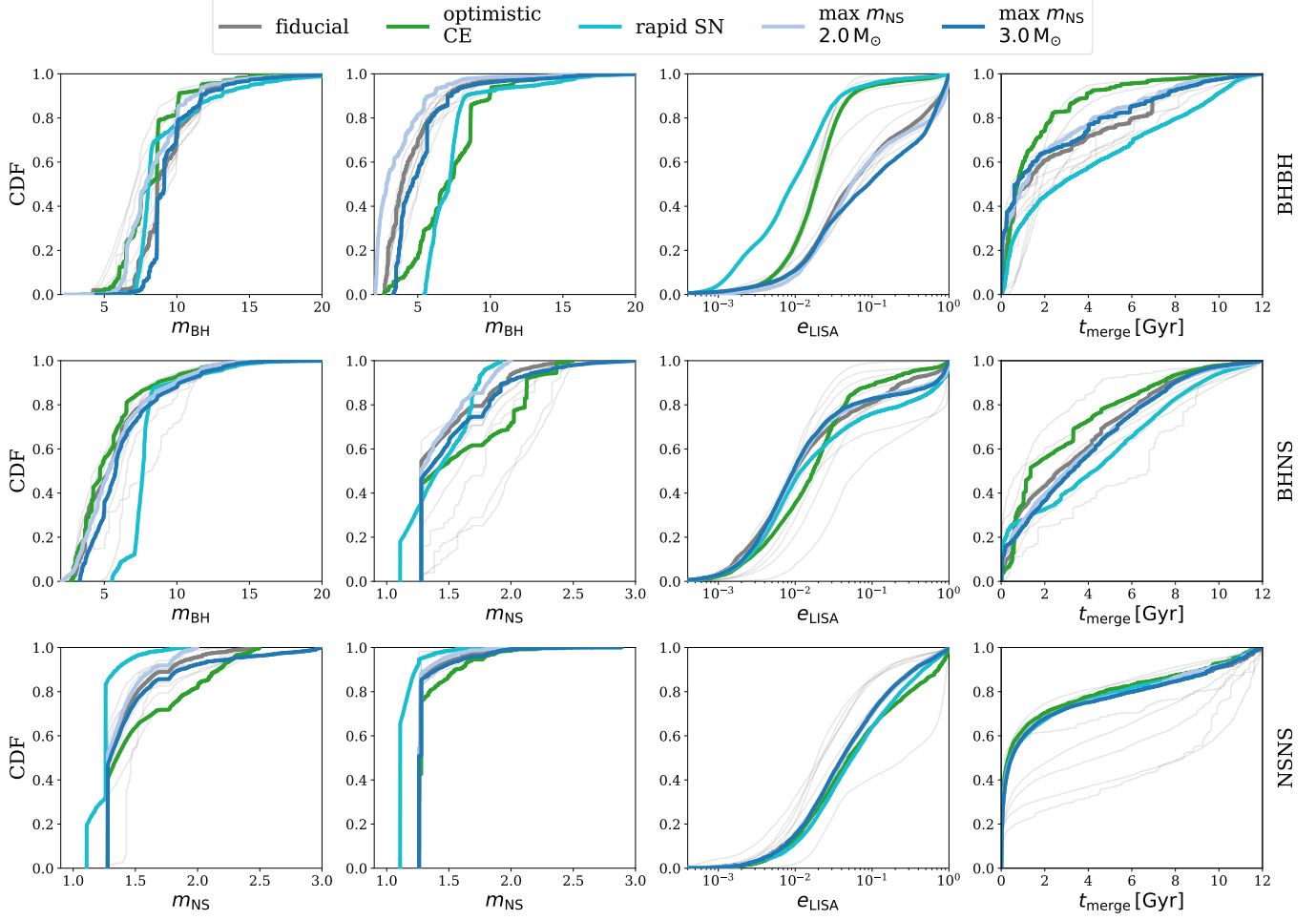


Figure 8. As Fig. 6, except comparing the fiducial population with models changing the maximum neutron star mass, remnant mass prescription and survivability of common envelope events initiated by Hertzsprung gap donors.

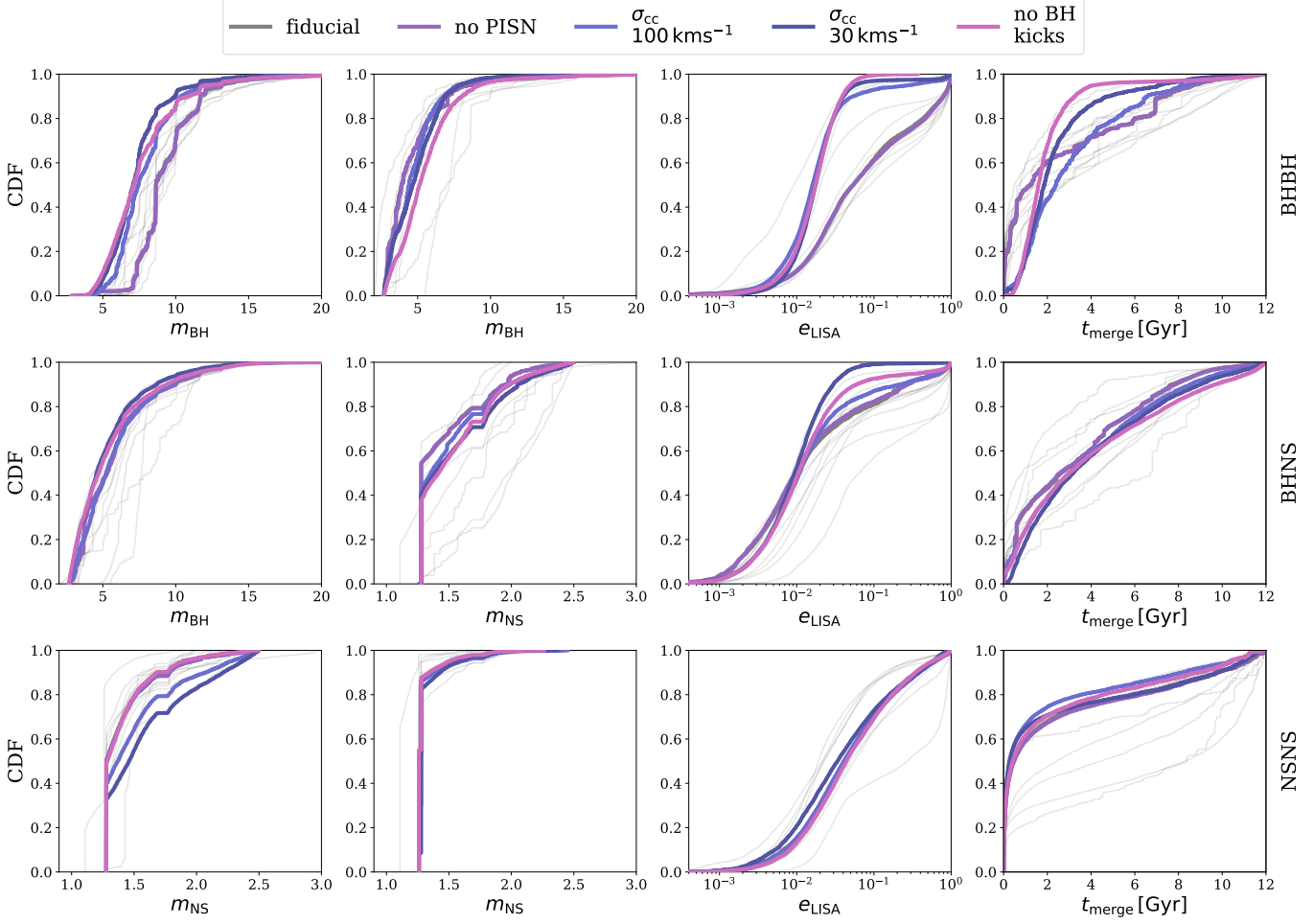


Figure 9. As Fig. 6, except comparing the fiducial population with models changing the core-collapse supernova kick distributions and the presence of BH kicks and PISNs.

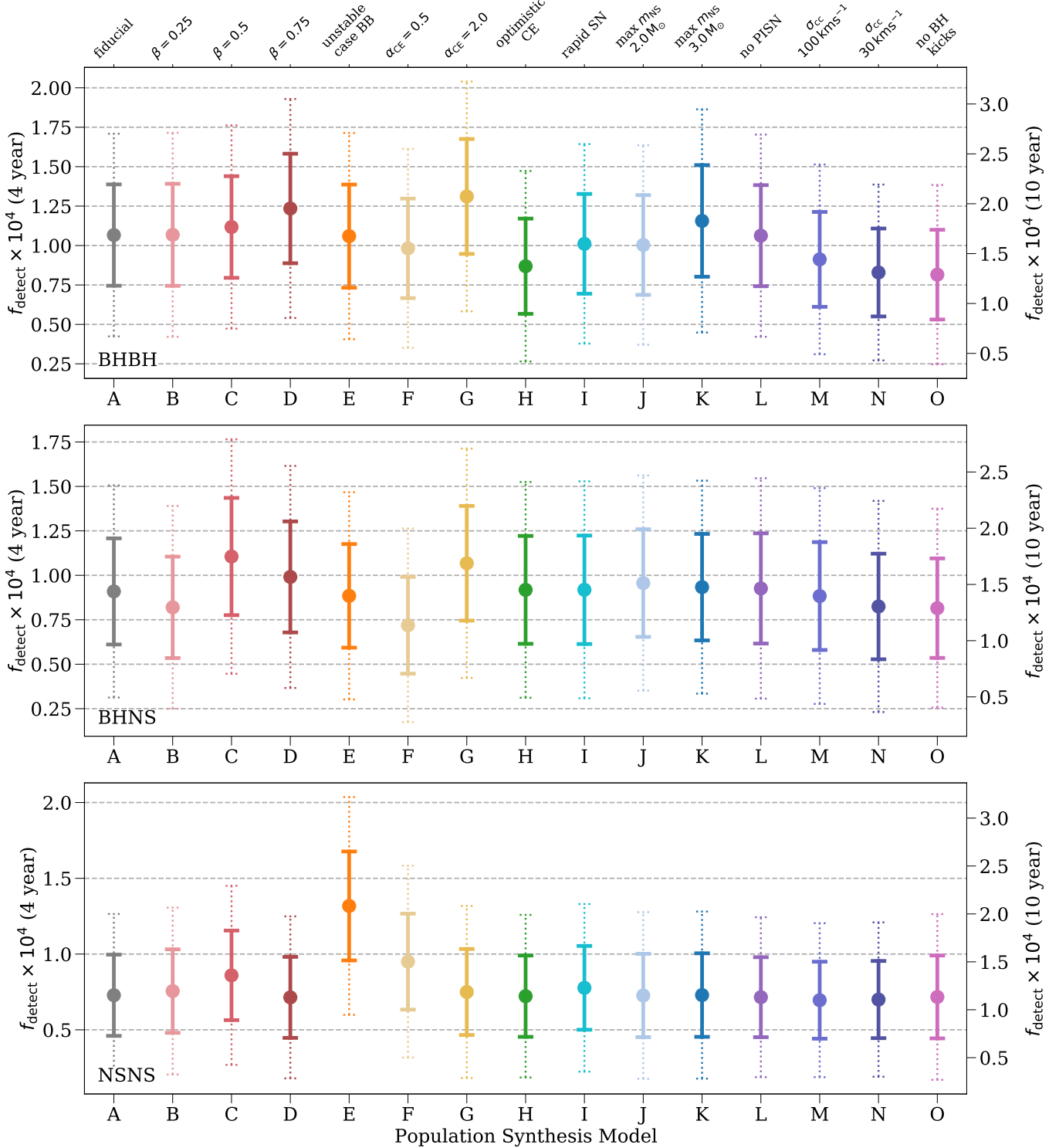


Figure 10. As Figure 3 except only showing the detectable fraction.

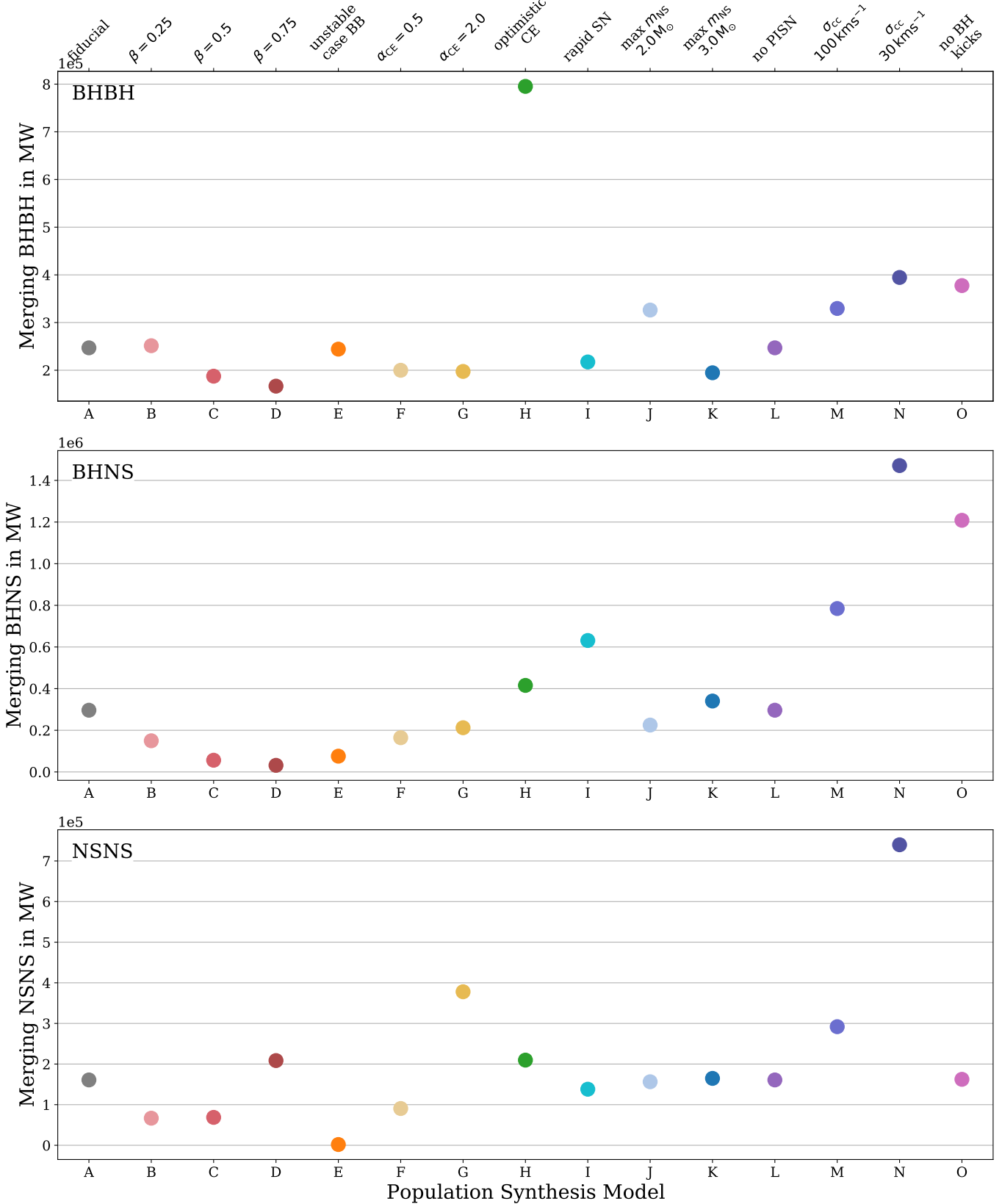


Figure 11. The total number of merging DCOs in the Milky Way. When multiplied by Figure 10 this gives Figure 3.

